Driving forces of the complex formation between highly charged disordered proteins

Aritra Chowdhury[a,1] (ID), Alessandro Borgia[a,2] (ID), Souradeep Ghosh[b] (ID), Andrea Sottini[a] (ID), Soumik Mitra[b] (ID), Rohan S. Eapen[a] (ID), Madeleine B. Borgia[a,2] (ID), Tianjin Yang[a], Nicola Galvanetto[a,c] (ID), Miloš T. Ivanović[a] (ID), Paweł Łukijańczuk[a] (ID), Ruijing Zhu[a], Daniel Nettels[a], Arindam Kundagrami[b,1] (ID), and Benjamin Schuler[a,c,1] (ID)

Highly disordered complexes between oppositely charged intrinsically disordered proteins present a new paradigm of biomolecular interactions. Here, we investigate the driving forces of such interactions for the example of the highly positively charged linker histone H1 and its highly negatively charged chaperone, prothymosin α (ProTα). Temperature-dependent single-molecule Förster resonance energy transfer (FRET) experiments and isothermal titration calorimetry reveal ProTα-H1 binding to be enthalpically unfavorable, and salt-dependent affinity measurements suggest counterion release entropy to be an important thermodynamic driving force. Using single-molecule FRET, we also identify ternary complexes between ProTα and H1 in addition to the heterodimer at equilibrium and show how they contribute to the thermodynamics observed in ensemble experiments. Finally, we explain the observed thermodynamics quantitatively with a mean-field polyelectrolyte theory that treats counterion release explicitly. ProTα-H1 complex formation resembles the interactions between synthetic polyelectrolytes, and the underlying principles are likely to be of broad relevance for interactions between charged biomolecules in general.

intrinsically disordered proteins | single-molecule spectroscopy | protein binding | polyelectrolyte complexation

Intrinsically disordered proteins (IDPs) can bind to many different cellular targets and are thus abundant in molecular interaction hubs (1–3). The underlying interaction mechanisms and the extent of disorder in IDP complexes cover a remarkably broad spectrum. For some IDPs, binding is coupled to folding and results in complexes with a well-defined three-dimensional structure (4). In other cases, some disorder is retained in the bound state (5, 6). For instance, IDPs often employ short secondary structure elements, small linear motifs, or even single-site modifications or side chains to engage interaction partners (7, 8). As a result, large parts of the chain can remain disordered. In extreme cases, one or both partners fully retain their structural disorder after binding, a mechanism that is particularly common for highly charged IDPs interacting with each other or with nucleic acids (9–13). We have recently identified such an example, the complex between the two human IDPs prothymosin α (ProTα) and linker histone H1 (13). ProTα and H1 carry large opposite net charges (–44 and +53, respectively) and associate into a heterodimer with picomolar to nanomolar affinity in the physiological range of salt concentrations, yet they retain their disorder in the complex. ProTα acts as a chaperone of H1 (14) and enables the dissociation of H1 from nucleosomes despite the extreme affinity of the H1-nucleosome complex (15).

The surprising absence of structure formation and of structured interaction interfaces in such disordered complexes raises the question of how the underlying thermodynamic driving forces for binding differ from the classical paradigms of interactions for folded proteins (16–18). In many respects, the interactions between highly charged naturally occurring biopolymers are reminiscent of the complexation between synthetic polyelectrolytes (9, 19–22). However, for synthetic systems, it has been challenging to experimentally probe the properties of small oligomers with well-defined stoichiometry separately from their phase separation by complex coacervation (23). The preparative biochemical methods and single-molecule spectroscopy available for biological polyelectrolytes provide an opportunity for closing this gap. Here, we dissect the thermodynamic driving forces involved in the formation of the dimer and the ternary complexes of ProTα and H1 under conditions where phase separation does not occur. We show that in spite of the high affinity, the interaction is enthalpically unfavorable and instead driven by the entropy gain from counterion release, as suggested for polyelectrolyte complexation (9, 19, 21, 22, 24–27).* Considering the abundance of

Significance

Charged disordered proteins are abundant in the cell, especially in the nucleus, and oppositely charged molecules can form high-affinity disordered complexes. Such interactions can exhibit surprising behavior, such as increased affinity with increasing temperature, but a detailed characterization of the underlying thermodynamic driving forces has been lacking. Combining single-molecule FRET (Förster resonance energy transfer), calorimetry, and analytical polymer theory, we dissect the thermodynamics of the disordered high-affinity complex between two highly charged disordered proteins and find that the release of counterions is an essential entropic contribution to binding. Our results also demonstrate the formation of higher-order complexes at high protein concentrations, and provide a quantitative experimental and theoretical framework for elucidating the interactions of charged disordered biomolecules and synthetic polyelectrolytes.

charges in IDPs and other biomolecules in the cell, the thermodynamic characteristics of the ProTα-H1 interaction are likely to resemble those of many biomolecular binding processes.

Results

High Affinity Despite Unfavorable Enthalpy. The most striking feature of the ProTα-H1 complex is that the two IDPs bind to each other with picomolar to nanomolar affinity in the physiological ionic strength range, although they both remain disordered in the complex (13, 28). To enable measurements at the very low protein concentrations where the equilibrium between monomers and the dimer of ProTα (P) and H1 (H) can be monitored, we use single-molecule Förster resonance energy transfer (FRET) on freely diffusing molecules with confocal detection (29–33). ProTα labeled with donor and acceptor fluorophores (Alexa Fluor 488 and 594, respectively) at positions 56 and 110 exhibits a FRET efficiency of 0.37 ± 0.03 at a monovalent salt concentration[†] of 208 mM. Upon titrating picomolar concentrations of labeled ProTα with increasing concentrations of unlabeled H1, we observe a second population corresponding to the ProTα-H1 dimer (PH) (Fig. 1A). Owing to the mutual charge screening of the two oppositely charged IDPs, ProTα is more compact in the complex (13), resulting in a higher transfer efficiency of 0.56 ± 0.03. The equilibrium fraction of PH as a function of H1 concentration allows us to determine the equilibrium dissociation constant, K_D^{PH} (Fig. 1B). K_D^{PH} increases from $2.1_{-0.8}^{+1.1}$ pM at 165 mM (13) to $1.2_{-0.6}^{+1.2}$ nM at 208 mM monovalent salt concentration.

To assess the role of enthalpic and entropic contributions to the binding process, we investigated the temperature dependence of K_D^{PH}. We measured transfer efficiency histograms of picomolar concentrations of labeled ProTα in the presence of a fixed concentration of unlabeled H1 close to K_D^{PH} between 283.5 K and 331 K (Fig. 1C). The temperature dependence reveals another remarkable feature of the PH complex: The equilibrium fraction of PH increases with increasing temperature, i.e., higher temperature favors binding (Fig. 1D). Correspondingly, ProTα-H1 complex formation must be associated with a thermodynamically unfavorable, positive enthalpy change, $\Delta H^{PH} > 0$. This conclusion is confirmed by isothermal titration calorimetry (ITC), which shows the signature of an endothermic reaction (Fig. 1E), as observed previously (34). Since $\Delta H^{PH} > 0$, ProTα-H1 binding must be entropically driven. This behavior contrasts with many high-affinity protein interactions, for which the enthalpy of binding is often favorable (17, 35). Notably, an unfavorable enthalpic contribution has also been observed for complex coacervation (10, 36, 37), indicating that the driving forces for phase separation of polyelectrolytes and for the formation of the ProTα-H1 dimer are closely related. The origin of the entropically dominated driving force of ProTα-H1 binding thus deserves closer investigation.

---

[*]The association of polyelectrolytes with oppositely charged macromolecules is loosely referred to as polyelectrolyte complexation in the literature (9, 19, 21, 22, 24–27), which is commonly used as an overarching term that refers to the formation of small oligomers (9, 12, 13, 46)—especially dimers (soluble complexes)—but also dense liquid phases (coacervates) (36, 85, 108–110), kinetically arrested states, such as layered structures (111, 112), and almost solid-like materials (41, 113–117) that can exhibit dynamical transitions (59, 118, 119) (nonequilibrium complexes).

[†]Unless otherwise mentioned, we used KCl to vary the salt concentration in the presence of a fixed concentration of 10 mM Tris buffer. "Monovalent salt concentration" represents the contributions of both components, i.e., the fixed concentration of ionized Tris–HCl (8 mM) and the concentration of KCl (see *Material and Methods* for details).
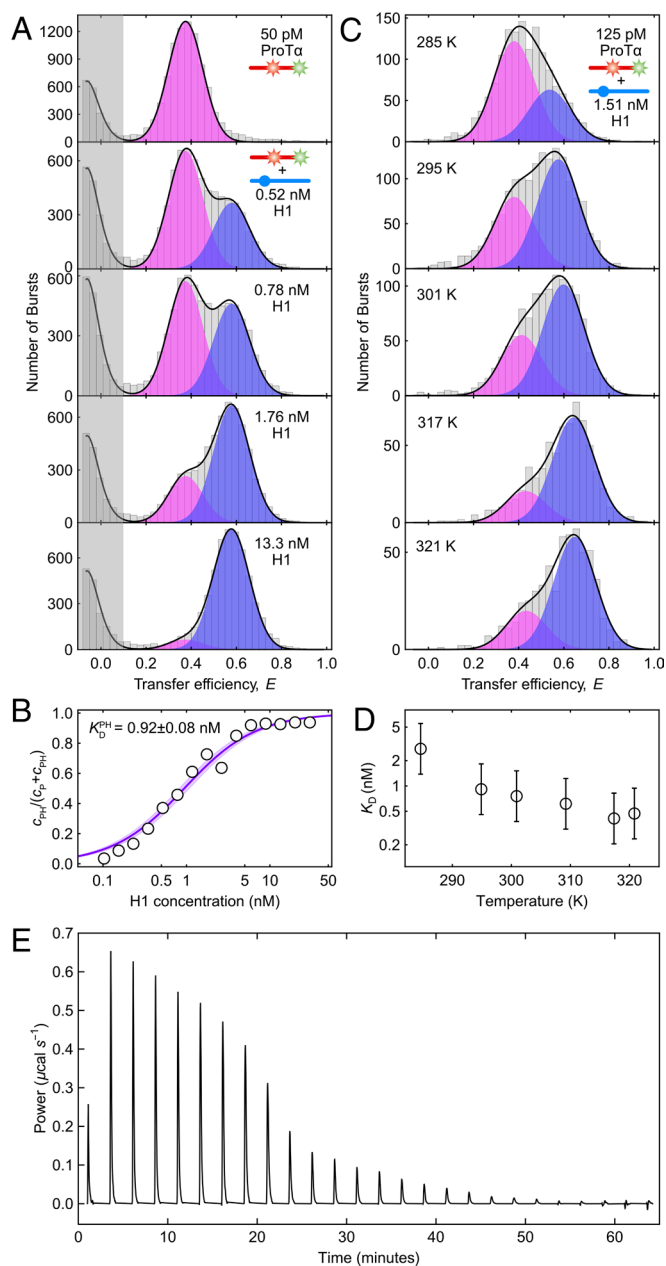

Fig. 1. The high-affinity binding between H1 and ProTα is endothermic. (A) Transfer efficiency histograms of 50 pM ProTα E56C/D110C labeled with Alexa Fluors 488 and 594 in the presence of increasing concentrations of unlabeled H1 (see the legend) at 208 mM monovalent salt concentration, globally fit with two Gaussian peak functions for the unbound (magenta) and bound (blue) ProTα populations, respectively (sum: black lines). (B) Representative example showing the bound fraction of labeled ProTα as a function of the H1 concentration fitted with a binding isotherm (solid line), in this case yielding an equilibrium dissociation constant of $K_D = 0.92 \pm 0.08$ nM (shaded band: 90% CI). (C) Transfer efficiency histograms of 125 pM ProTα E56C/D110C labeled with Alexa Fluor 488/594 in the presence of 1.51 nM unlabeled H1 at 208 mM monovalent salt concentration, measured at different temperatures and fitted with two Gaussian peak functions for the unbound (magenta) and bound (blue) ProTα populations, respectively (sum: black lines). (D) The resulting temperature-dependent K_D shows rising affinity with increasing temperature, thus endothermic binding. Error bars represent a conservative systematic error of a factor of 2 on K_D (*SI Appendix*). (E) ITC thermogram, showing differential power as a function of time upon titrating ProTα into H1 at 208 mM monovalent salt concentration, which confirms endothermic binding.

Counterion Release Entropy Is a Strong Driving Force for ProTα-H1 Binding. Naively, it might be tempting to envision the driving force for binding between oppositely charged macromolecules in terms of simple Coulomb attraction between them. However, in this case, the process should be exothermic, in contrast to what we observe
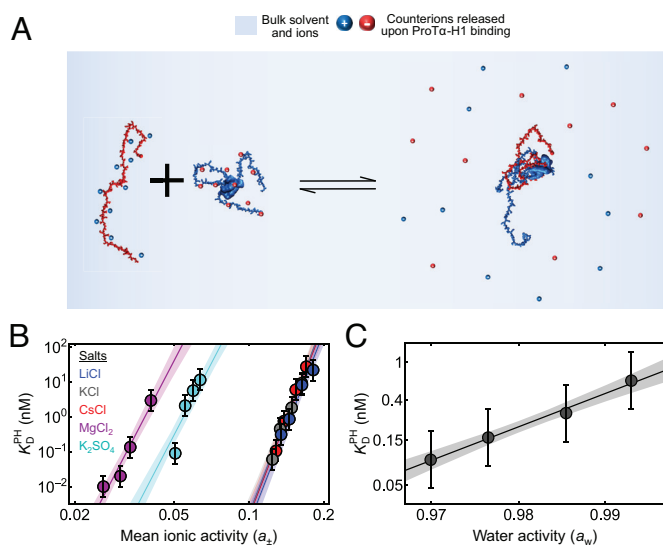
A

Fig. 2. Effects of ion and water activities on ProTα-H1 binding. (*A*) Schematic of ProTα binding to H1 associated with counterion release. (*B*) Equilibrium dissociation constant for ProTα-H1 binding, K_D^{PH}, at different mean ionic activities ($a_\pm$) of various salts (see the legend for color code). The data are fitted globally to obtain the number of monovalent and/or divalent ions released upon ProTα-H1 complex formation (see *SI Appendix* for details). The solid lines represent the fit, and the shaded regions represent 90% CIs. (*C*) K_D^{PH} at 208 mM monovalent salt concentration as a function of water activity (a_w), varied by changing the concentration of the osmolyte triethylene glycol (*SI Appendix*). The solid line represents a fit with Eq. **4** for estimating the apparent number of water molecules released upon ProTα-H1 complex formation (shaded band: 90% CI). All error bars represent a conservative systematic error of a factor of 2 on K_D (*SI Appendix*).

for H1 and ProTα. This simple picture ignores the essential role of counterions, present in the solution to ensure electroneutrality, and some of which associate with polyelectrolytes due to Coulomb attraction (19, 24). The presence of ions can extensively modulate biomolecular conformations, dynamics, and recognition (38–40), but the effects become particularly pertinent when two polyelectrolyte chains associate (be they biological or synthetic): Counterions are released into solution as charge interactions form between the chains, which results in a gain in translational entropy owing to the dilution of the ions into the bulk solution (Fig. 2*A*). This favorable counterion release entropy has been suggested to be a key driving force for polyelectrolyte complexation (24, 41–43). To quantify the contribution of counterions, Record and Lohman (24) developed an approach based on the principles of coupled equilibria between biomolecular binding and counterion release. In our case, unbound ProTα and H1 are associated with their counterions to attain charge neutrality; upon H1 binding to ProTα, n_- of the previously associated monovalent anions (A⁻) and n_+ of the monovalent cations (C⁺) are released:

$$\text{ProT}\alpha + \text{H1} \rightleftharpoons \text{ProT}\alpha\text{-H1} + n_+\text{C}^+ + n_-\text{A}^-. \qquad [1]$$
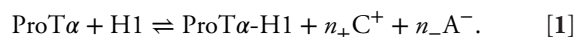
However, n_+ and n_- can usually not be observed directly. Instead, we probe the apparent equilibrium

$$\text{ProT}\alpha + \text{H1} \overset{K_D^{PH}}{\rightleftharpoons} \text{ProT}\alpha\text{-H1}. \qquad [2]$$
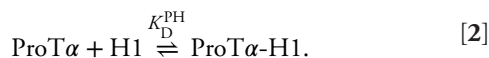
Record and Lohman (24) related the dependence of the corresponding observed equilibrium dissociation constant, K_D^{PH}, on the mean ionic activity of the participating ions, $a_\pm$, to the total number of counterions released, Δn:

$$\Delta n = n_+ + n_- \approx \frac{d\log K_D^{PH}}{d\log a_\pm}. \qquad [3]$$

For H1 binding to ProTα, this dependence on salt concentration is remarkably strong: K_D^{PH} increases by six orders of magnitude (from $2.1^{+1.1}_{-0.8}$ pM to 4 ± 2 μM) between 165 mM and 340 mM monovalent salt (13, 28). Eq. **3** yields a release of 18 ± 1 monovalent counterions upon complex formation (13, 28), an unusually large number compared to other biomolecular systems (24, 44).

To assess the effect of the chemical identity of the counterions and their charge on the process, we extended this analysis to other chloride salts of monovalent cations (LiCl and CsCl) as well as divalent cations and anions [K₂(SO₄) ad MgCl₂] (Fig. 2*B*). Effects of ions on polyelectrolyte complexation and biomolecular recognition can be complex, including the coupling of ion-specific conformational transitions to binding (45), differential ion uptake and release (46), and the ion-driven modulation of hydration effects (47). In the simplest scenario, however, the total number of anionic and cationic charges that are released upon binding to warrant charge neutrality is independent of the valence and identity of the counterions—this indeed seems to be the case for the binding of ProTα to H1: For the monovalent salts tested, the results are independent of chemical identity (Fig. 2*B*), suggesting that their interactions with the protein are nonspecific. For the divalent salts, the total number of released ions should be lower than for monovalent salts. Indeed, we observe a reduced slope for the dependence of log K_D^{PH} vs. log $a_\pm$ for salts with divalent cations or anions (Fig. 2*B*). From a global fit of the dependencies of K_D^{PH} on mean ionic activity for all five salts with a generalization of Eq. **3** (*SI Appendix*), we obtain 18 ± 1 for the sum of positive and negative charges released upon binding (Fig. 2*B*), respectively, consistent with our previous estimate of 18 ± 1 monovalent counterions released (13, 28). A general caveat of this analysis lies in the assumption that the extent of counterion adsorption is independent of salt concentration (24), which may not be fully realistic for flexible polyelectrolytes (48). Nevertheless, we can conclude that a large number of counterions is released when H1 binds to ProTα, and the resulting gain in their translational entropy is a driving force of complex formation (24, 41, 42).

Another contribution to binding processes originates from hydration (24, 49–51). These effects are more difficult to interpret mechanistically (52), but we assessed the role of water in ProTα-H1 complex formation by varying the water activity, a_w, with a neutral small-molecule osmolyte, triethylene glycol (53) (*SI Appendix*), and measuring its influence on K_D^{PH}. Formally, this result can be expressed in terms of the number of water molecules released upon complex formation, Δn_w, according to (51, 53)

$$\Delta n_w \approx \frac{d\log K_D^{PH}}{d\log a_w}, \qquad [4]$$

yielding $\Delta n_w = 80 \pm 5$ (Fig. 2*C*). For comparison, for folded proteins binding specifically to their cognate double-stranded DNA targets, Δn_w is considerably larger, typically with hundreds and up to ~1,000 water molecules released upon complex formation (47, 53–55). The lower value of Δn_w for ProTα-H1 binding is not entirely surprising since the IDPs remain highly hydrated owing to the disordered nature of the complex (13). Relating Δn_w to simple thermodynamic quantities is complicated by the many degrees of freedom involved in hydration

processes (52), but the free energy gain from the entropy of dilution is expected to be low because of the high bulk concentration of water (~55.5 M).

A final contribution to consider is configurational entropy of the polypeptide chains, which can play an important thermodynamic role in binding reactions of IDPs, for instance, if they are coupled to folding (56). In the case of H1 and ProTα, however, both IDPs retain their disorder and chain dynamics in the bound state (13), and the chains undergo only a minor compaction (Fig. 1A and *SI Appendix*, Fig. S1). Other degrees of freedom may contribute (18) but are difficult to identify unequivocally and are likely to be model-dependent. Based on a simple Gaussian chain model and a compaction by 23% in terms of end-to-end distance for ProTα at 208 mM monovalent salt concentration (*SI Appendix*, Fig. S1), we estimate a total change in configurational free energy of ~0.5 k_BT upon binding, assuming similar compaction for both ProTα and H1; this contribution is negligible compared to the total free energy of binding of ~20 k_BT.

Altogether, we thus conclude that counterion release entropy is likely to be a strong thermodynamic driving force for PH formation, as for polyelectrolyte complexation of synthetic systems (24, 41, 42), whereas changes in chain entropy of the IDPs are negligible for such a highly disordered complex. Contributions from hydration to the free energy of binding are likely to be relevant (57) but difficult to dissect into enthalpic and entropic contributions experimentally.

Resolving Ternary Complex Formation at Higher Protein Concentrations. So far, we have focused on the dimerization equilibrium P + H ⇌ PH, which describes the interaction between H1 and ProTα at picomolar and low nanomolar protein concentrations in the physiological ionic-strength range (13, 28). However, several observations indicate the existence of larger oligomers. First, transfer efficiencies and hydrodynamic radii for ProTα-H1 complexes were found to exhibit a continuous and progressive shift at large excess of one of the binding partners (13). Second, the interaction kinetics of H1 and ProTα are protein concentration-dependent and

deviate from two-state behavior at high nanomolar protein concentrations and above (28), a signature of the formation of ternary complexes, such as ProTα₂-H1 (PPH) and ProTα-H1₂ (PHH) (58). The presence of ternary complexes also explains the fast exchange between bound and unbound states when the reaction is probed at the micromolar concentrations required for NMR spectroscopy (28). Third, molecular simulations demonstrate that the disordered nature of the complex facilitates the formation of higher-order oligomers (13, 15, 28). To probe the properties of ternary complexes more directly, we reasoned that since the interactions are charge-driven, reducing the salt concentration should further increase the affinity and decrease the kinetic exchange rates for the ternary complexes and might thus enable the detection of ternary complexes at equilibrium.

The existence of species beyond monomers and dimers does indeed become obvious in single-molecule titration experiments at low salt and elevated concentrations of unlabeled protein as distinct subpopulations in the transfer efficiency histograms (Fig. 3 A and B). For instance, we mixed 10 nM unlabeled ProTα and H1 each at 62 mM monovalent salt concentration and doped it with 70 pM labeled P as a probe that partitions between all ProTα-containing species and reports on their equilibrium fractions (Fig. 3A). Initially, a single population corresponding to the ProTα-H1 dimer is observed. If P + H ⇌ PH was the only contributing process, adding excess unlabeled P would simply cause a decrease in the observed equilibrium fraction of PH and an increase in the fraction of P. Instead, the decrease in the fraction of PH is accompanied by the appearance of a separate population with a transfer efficiency between those of PH and P. This new population reaches its maximum at a P:H stoichiometry of ~2:1, as expected for the ternary complex PPH. Adding even higher excess of P decreases the fraction of PPH, concomitant with an increase in the fraction of unbound P. From the fractions of PH and PPH, we obtain $K_D^{PPH} = 0.7^{+0.7}_{-0.4}$ nM for the reaction PPH ⇌ PH + P (Fig. 3C).

Analogously, we can populate the ternary complex PHH in experiments with an excess of H1. Fig. 3B shows a titration starting from
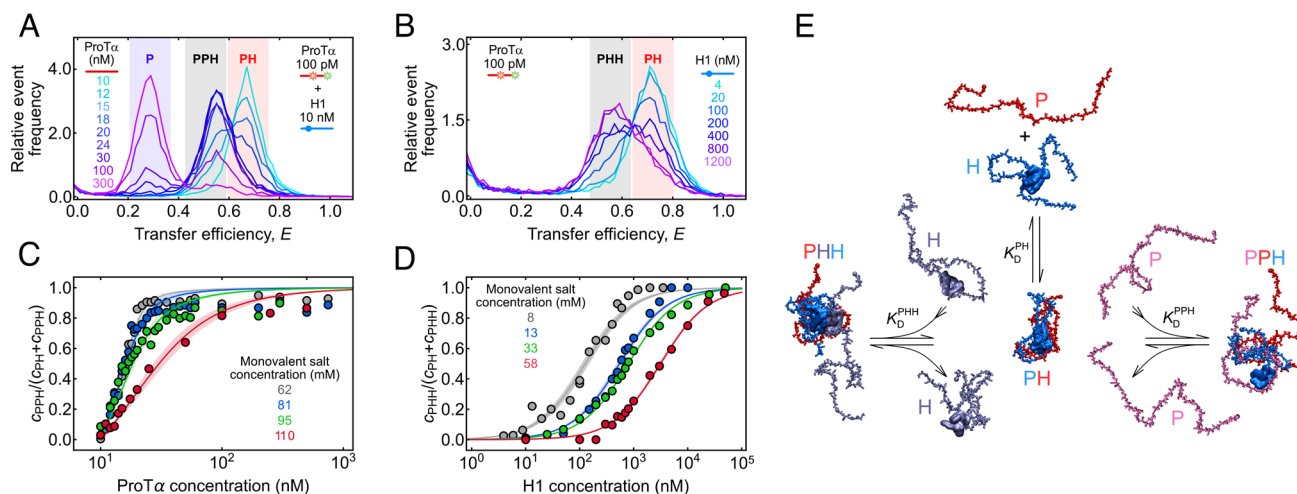

Fig. 3. Resolving ternary complexes with single-molecule spectroscopy at equilibrium. (A) Overlay of transfer efficiency histograms of 100 pM ProTα E56C/D110C labeled with Alexa Fluors 488/594 at 62 mM monovalent salt concentration in the presence of 10 nM unlabeled H1, with increasing concentrations of unlabeled ProTα (see legend), showing the formation of the PPH ternary complex as a separate peak. The red-, gray-, and purple-shaded regions indicate the peaks corresponding to PH, PPH, and unbound P, respectively. (B) Overlay of transfer efficiency histograms of 100 pM ProTα E56C/D110C labeled with Alexa Fluors 488/594 at 8 mM monovalent salt concentration, with increasing concentrations of unlabeled H1 (see legend), showing the formation of the PHH ternary complex as a separate peak. The red- and gray-shaded regions indicate the peaks corresponding to PH and PHH, respectively. (C and D) Fraction of ternary complexes, PPH (C) or PHH (D), as a function of unlabeled ProTα (C) or H1 (D) concentration at different monovalent salt concentrations (see legend) from the type of titrations shown in A and B. Solid lines represent fits with binding isotherms (*SI Appendix*); shaded regions indicate 90% CIs. (E) Schematic of ProTα (red, pink) and H1 (blue, purple) forming the PH dimer and PHH and PPH ternary complexes, using snapshots from coarse-grained simulations (59).

70 pM labeled ProTα saturated with 3 nM unlabeled H1 at a monovalent salt concentration of 8 mM (originating from the buffer alone), which results in a single population corresponding to the ProTα-H1 dimer. Upon adding more unlabeled H1, however, an additional population with lower transfer efficiency appears and increases with H1 concentration, corresponding to PHH. From the H1-dependent fraction of PHH, we obtain $K_D^{PHH} = 0.12^{+0.12}_{-0.06}$ μM for the reaction PHH ⇌ PH + H (Fig. 3D). These titration experiments thus not only allow us to resolve the ternary complexes PPH and PHH at equilibrium but also to quantify their stability.

With this approach, we can also probe the sensitivity of K_D^{PHH} and K_D^{PPH} to salt concentration and assess the role of counterion release for ternary complex formation (Fig. 4A). For both K_D^{PHH} and K_D^{PPH}, the highest experimentally accessible salt concentrations are

limited by the decreasing separation between dimers and ternary complexes in the transfer efficiency histograms, which prevents assignment of the different species at high salt (Fig. 3 A and B); for K_D^{PPH}, the lowest accessible salt concentrations were limited by complex coacervation of ProTα and H1 occurring even at nanomolar protein concentrations (60). Nevertheless, extrapolating the salt concentration dependencies of K_D^{PH}, K_D^{PPH}, and K_D^{PHH} affords a systematic comparison of the free energies of formation for PH (ΔG^{PH}), PPH (ΔG^{PPH}), and PHH (ΔG^{PHH}). Across the experimentally accessible range, the absolute values of the free energies follow the order $|\Delta G^{PH}| > |\Delta G^{PPH}| > |\Delta G^{PHH}|$; i.e., PH is most stable, followed by PPH and PHH (Fig. 4A).

The slopes of the three salt concentration dependencies, however, are very different. Using Eq. 1, we can estimate the numbers of counterions released upon formation of PPH and PHH,
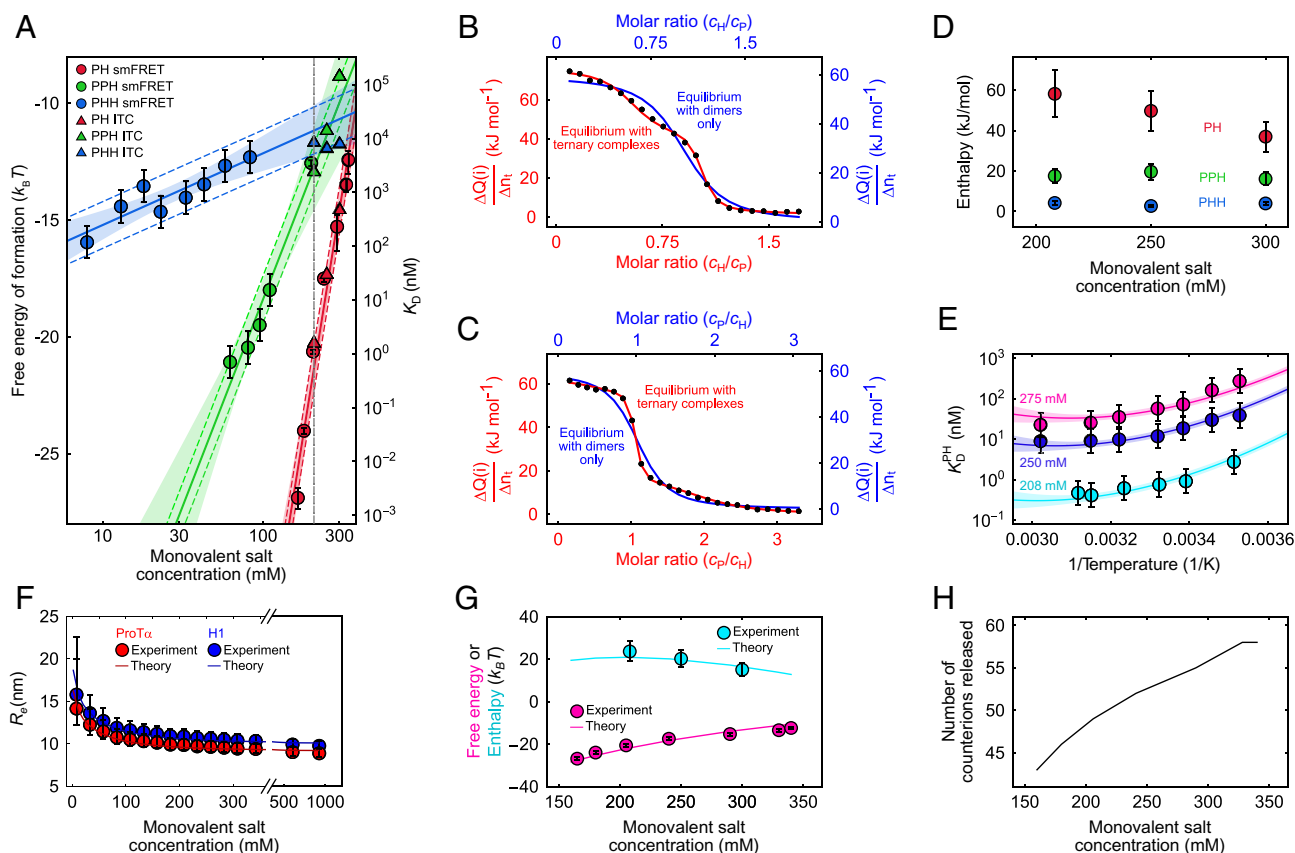

Fig. 4. Thermodynamics of ProTα-H1 binding including ternary complex formation. (A) Free energies and dissociation constants of forming PH dimers (red) and the ternary complexes PPH (green) and PHH (blue) from single-molecule FRET (circles; including previously published data (13, 59)) and ITC (triangles; see *SI Appendix*, Fig. S2, for titrations) as a function of monovalent salt concentration and fits with Eq. 3 (or analogous for PPH and PHH, solid lines; shaded bands: 90% CIs). Error bars on single-molecule data for PH are from Borgia et al. (13); for PHH and PPH, error bars represent a conservative systematic error of a factor of 2 on K_D (*SI Appendix*). Colored dashed lines represent ±1 $k_B T$ from the fit lines, the upper bound estimated for the perturbation from dye labeling (59). The vertical dashed gray line indicates a monovalent salt concentration of 208 mM. (B and C) Integrated power from ITC per molar amount of injected titrant ($\Delta Q / \Delta n_t$; black points for each injection i) as a function of the molar ratio of both proteins, upon titrating H1 into ProTα (B) and ProTα into H1 (C) at 208 mM monovalent salt concentration. The data in (B) and (C) are globally fitted either with a 1:1 binding model (blue line and blue axis labels) or with a model including PHH and PPH ternary complexes (red line and red axis labels) (see *SI Appendix* for details; note that the molar ratio is a fit parameter and thus slightly different for the two analyses). (D) Enthalpies of forming PH (red), PPH (green), and PHH (blue) from the ITC analysis (B and C and *SI Appendix*, Fig. S2) as a function of monovalent salt concentration. Error bars of ±20% are from the constraints on the protein concentrations used in fitting (*SI Appendix*, Table S2). (E) Temperature dependence of ProTα-H1 dissociation constants from single-molecule FRET measurements, shown as Van 't Hoff plots, at 208 mM (cyan), 250 mM (blue), and 275 mM (magenta) monovalent salt concentration. Error bars represent a conservative systematic error of a factor of 2 on K_D (*SI Appendix*). All three datasets are fitted globally with the integral form of the Van 't Hoff equation (solid lines; *SI Appendix*), with the heat capacity change upon binding as a shared fit parameter (*SI Appendix*; shaded bands: 90% CIs). (F) Salt dependence of the average end-to-end distance, R_e, for ProTα (red circles) and H1 (blue circles). R_e for ProTα was measured using single-molecule FRET; for H1, it is approximated using the scaling exponents for ProTα (see *SI Appendix* for details). Error bars are estimated from a conservative systematic error of ±0.03 on transfer efficiencies. The blue and red lines show R_e for ProTα and H1, respectively, using the theory for single isolated polyelectrolyte chains (see *SI Appendix* for details). (G) Comparison of the experimental free energy (magenta circles) and enthalpy (cyan circles) of ProTα-H1 complex formation as a function of monovalent salt concentration with those estimated from the theory of polyelectrolyte complexation (magenta and cyan lines for enthalpy and free energy, respectively; see *SI Appendix* for details). Error bars on experimental free energy and enthalpy as in (A) and (D). (H) The number of counterions released upon PH formation from the theory of polyelectrolyte complexation (see *SI Appendix* for details).

yielding values of 8 ± 1 and 1.3 ± 0.3, respectively (Fig. 4*A*), much lower than the value of 18 ± 1 for PH formation. Evidently, the largest charge compensation and counterion release occurs during formation of PH, corresponding to the largest driving force among the three complexes. The ProTα-H1 dimer has a nominal net charge of +9 owing to the higher net charge of H1 (+53) compared to ProTα (–44); adding another ProTα chain thus yields substantial further charge compensation and counterion release. In contrast, adding H1 to the dimer is electrostatically much less favorable and leads to little counterion release. Extrapolation to 208 mM monovalent salt concentration (Fig. 4*A*) yields values of the dissociation constants of $K_D^{PPH} = 3^{+14}_{-2}$ µM and $K_D^{PHH} = 13^{+26}_{-9}$ µM. The presence of ternary complexes[‡] must thus be taken into account for the quantitative interpretation of any experiment performed in the micromolar protein concentration range.

Quantifying Enthalpic Contributions in ProTα-H1 Complex Formation. Calorimetric measurements are considered the gold standard of thermodynamic analysis because they afford the direct measurement of binding enthalpies (61). However, since ITC cannot directly detect how many or which molecular species contribute, the accurate interpretation of the measured reaction heats requires an appropriate model comprising all equilibria involved. A semiempirical analysis of ITC measurements under conditions where both coacervation and soluble complex formation contribute have previously been used to infer positive enthalpies of ion pairing between polyelectrolytes (10, 36, 37). Here, we take the thermodynamic analysis one step further by performing measurements at sufficiently low protein concentrations so that phase separation does not contribute (60) and by explicitly accounting for the binding equilibria of dimers and ternary complexes of H1 and ProTα. Our detailed dissection of the ProTα-H1 interaction based on single-molecule FRET experiments over a wide range of protein and salt concentrations now allows us to approach such a complete thermodynamic analysis of ITC measurements. We performed ITC experiments at three different KCl concentrations corresponding to monovalent salt concentrations of 208 mM, 250 mM, and 300 mM, each with ProTα as a titrant (material injected) and H1 as a titrand (material in the sample cell) and vice versa (Fig. 4 *B* and *C* and *SI Appendix*, Fig. S2). Quantitative analysis of ITC measurements at lower salt concentrations was impeded by liquid–liquid phase separation (60).

The ITC titrations measured at 208 mM monovalent salt concentration, when fitted with a binding model involving only dimer formation, P + H ⇌ PH, yield apparent micromolar dissociation constants (34) (*SI Appendix*, Fig. S2 and Table S1) but show obvious deviations from the experimental data, reflecting the inadequacy of the model (Fig. 4 *B* and *C* and *SI Appendix*, Fig. S2). This result is not unexpected since the ITC measurements require micromolar protein concentrations, where both the dimer and the ternary complexes need to be considered. At 208 mM monovalent salt concentration, e.g., we expect that for 15 µM H1 and 45 µM ProTα, ~84% of the complexes are PPH. We thus include all three coupled equilibria, P + H ⇌ PH, PH + P ⇌ PPH, and PH + H ⇌ PHH, with their corresponding dissociation constants and reaction enthalpies K_D^{PH} and ΔH^{PH}, K_D^{PPH} and ΔH^{PPH}, and K_D^{PHH} and ΔH^{PHH},

respectively, as fit parameters, in a global analysis of the ITC measurements (see *SI Appendix* for details). We constrain the dissociation constants to be in agreement with the values extrapolated from the single-molecule data (binding free energies within ~1 $k_B T$, Fig. 4*A* and *SI Appendix*, Table S2) and obtain a good fit at all salt concentrations (Fig. 4 *A–C* and *SI Appendix*, Fig. S2). Taking into account ternary complex formation thus reconciles the apparent discrepancy between K_D^{PH} obtained from single-molecule FRET (13, 28) and ITC (34) (Fig. 4*A* and *SI Appendix*, Fig. S2).

Our ITC analysis yields positive values for ΔH^{PH}, ΔH^{PPH}, and ΔH^{PHH}; thus, not only dimerization but also ternary complex formation must be entropically driven. ΔH^{PH} is the largest among the three reaction enthalpies and decreases with monovalent salt concentration, from 58 ± 12 kJ mol^{-1} at 208 mM to 35 ± 7 kJ mol^{-1} at 300 mM (Fig. 4*D*). Electrostatic interactions, be they counterion accumulation near charged side chains of H1 and ProTα, or attraction between charged side chains in H1 and ProTα, are per se exothermic. However, if counterion condensation is more exothermic than the electrostatic attraction between the two IDPs, then the overall complex formation process can be endothermic. This hypothesis is compatible with the decrease in ΔH^{PH} with increasing salt concentration, where charge screening is expected to attenuate the exothermicity of the underlying microscopic processes. Additional contributions may originate from ion-water interactions (41). In summary, while counterion release entropy is a strong overall driving force for ProTα-H1 complex formation, the enthalpy of binding is likely to be determined by competing differential side chain–ion and side chain–side chain interactions.

To complete the thermodynamic characterization of ProTα-H1 binding, we extended our analysis to the temperature dependence of K_D^{PH} from the single-molecule FRET measurements at different salt concentrations (Figs. 1 *C* and *D* and 4*E*). The resulting Van 't Hoff plots show a small yet consistent curvature for all datasets, indicating a temperature dependence of ΔH^{PH} and the reaction entropy, ΔS^{PH}. The corresponding change in heat capacity upon binding, ΔC_p, can be obtained from a fit with the integrated form of the Van 't Hoff equation (*SI Appendix*). Using ΔH^{PH} from the ITC measurements[§], we fit all datasets with ΔC_p as a global fit parameter, yielding a value of –1.6 ± 0.3 kJ mol^{-1} K^{-1} (Fig. 4*E*). Identifying the molecular origins of ΔC_p is far from trivial, with potential contributions from different factors, including a differential temperature dependence of hydration for charged side chains and ions (62), but the small value of ΔC_p is typical of biomolecular binding and contrasts with the larger values associated with protein folding (63), where hydrophobic interactions are expected to make a larger contribution. The nonzero ΔC_p reflects some entropy–enthalpy compensation across different salt concentrations, resulting in a modest sensitivity of ΔG^{PH} to temperature, in contrast to the dramatic sensitivity of ΔG^{PH} to salt concentration. We can thus conclude that at the physiological temperature of 37 °C, PH complex formation is enthalpically unfavorable over a broad range of salt concentrations, up to ~350 mM, and counterion release is an important entropic driving force.

A Polymer Model of Polyelectrolyte Dimer Formation. We employed an analytical polyelectrolyte model incorporating counterion condensation and uniform expansion (64–66),

---

[‡]Note that we cannot exclude the population of higher oligomers in the presence of a large excess of binding partners if their transfer efficiencies are within experimental uncertainty of the ternary complexes. However, since K_D^{PPH} and K_D^{PHH} are orders of magnitude higher than K_D^{PH}, the analogous dissociation constants for higher-order complexes are likely to be much greater (28) and their contribution to the measurements correspondingly small. The dimerization of PH to dimers of dimers in the protein concentration range we use is incompatible with pulsed field gradient NMR and two-focus FCS measurements (13). We thus use the simplest model that consistently describes all experimental data.

[§]Either using ΔH^{PH} from ITC at 276 K (for 208 and 250 mM monovalent salt concentration) or estimated from a linear extrapolation of the measured ΔH^{PH} as a function of monovalent salt concentration (for 275 mM monovalent salt concentration, where ITC was not measured).

based on the Edwards–Muthukumar Hamiltonian (48, 67–69), to quantitatively describe the driving forces of the ProTα-H1 interaction. This theory of polyelectrolyte complexation takes into account conformational properties of the individual IDPs, IDP-associated counterions, and salt ions free in solution, resulting in various contributing free energy components: the translational entropy of IDP-associated and free counterions (referred to as F_1 and F_2, respectively, in *SI Appendix*); the electrostatic free energy due to the spatial correlations between free ions (F_3); the energy of ion-pairing for chain-counterion and interchain charge interactions (F_4); and the conformational free energy of the IDPs (F_5). For two complexing IDPs characterized by their respective degrees of polymerization and net charges (N_1, N_2, and N_{c1}, N_{c2}, respectively), intra- and interchain excluded-volume interaction strengths (w_0) as well as local dielectric mismatch parameters (δ_0 for chain-counterion and δ_{12} for chain–chain ion-pairing), the total free energy is self-consistently minimized with respect to chain dimensions and the number of adsorbed counterions, and this is done for different salt concentrations for the complexed state and the unbound states (64, 65) (see *SI Appendix* for details).

While free salt ions have an ideal-gas-like entropy in the system volume (F_2), bound counterions have substantially reduced translational entropy (F_1) since they are assumed to remain confined to a cylindrical volume along the chain contour. The electrostatic free energy among the free ions (F_3) is captured by a parametrically corrected Debye–Hückel theory using a multiplicative factor, Λ (see *SI Appendix*, Fig. S3 for details). There is a gain in ion-pairing energy (F_4) due to counterion condensation on the chains as well as from interchain ion-pairing. IDPs with charged segments contribute to the configurational entropy, excluded-volume interactions, and screened Coulomb interactions (F5). Upon chain complexation, counterions associated with the complexed parts of the chains are assumed to be released into the system volume, gaining translational entropy, while the dangling uncomplexed parts of the longer chain retain their adsorbed counterions.

Although the model takes into account the entropy and enthalpy of counterions and their interactions with the protein chains, and thus charge renormalization, it lacks an explicit description of charge patterning (18, 70) and charge regulation in terms of side chain pK_a shifts (71, 72), and it also uses a parametric correction for the free energy of ionic correlations instead of a formal description of this correlation energy (73) as a function of salt concentration. Charge regulation is likely to be negligible in the salt concentration range where we studied ProTα-H1 complex formation experimentally (see *SI Appendix* for details and *SI Appendix*, Fig. S4) (74, 75) and is therefore inconsequential for the interpretation of theoretical thermodynamic estimates; however, the estimates of the single-chain dimensions are slightly affected at low salt concentrations (see *SI Appendix* for details and *SI Appendix*, Fig. S4). The uniform net charge density assumed in the theory is likely to limit its applicability to highly charged polyelectrolytic sequences such as ProTα and H1. Hydration effects and solvent degrees of freedom (57, 62, 76) are beyond the scope of this type of theory. Nevertheless, the implicit solvent model of our approach accounts for some hydration effects in the enthalpic terms describing the protein–protein and protein–ion interactions, primarily by considering a local dielectric constant near the protein surface that can be different from the bulk, as supported by fluorescence spectroscopy with polarity-sensitive probes (77, 78); the theory approximates the distance dependence of the dielectric constant as a step function and assumes ion pairing to be represented by fixed dipoles as a simple approximation. Furthermore, the dielectric mismatch parameter serves as a single mean-field parameter that comprises two microscopic aspects of ion-pairing: a local dielectric constant and the effective dipole length, so it does not allow either parameter to be determined independently (see *SI Appendix* for details).

We parameterized the theory based on the experimental salt concentration-dependent observables—chain dimensions of ProTα and H1 and thermodynamic parameters for complex formation of ProTα-H1—using a sequential approach. An estimate of w_0 was obtained from the single-chain dimensions at high salt, where charge interactions are screened, and constraints on δ_0 were estimated based on the chain dimensions and their experimental uncertainty at low salt; subsequently, using the estimated value of w_0, we fitted the experimental thermodynamic observables (enthalpy and free energy of complexation) by systematically varying δ_0 (within the constraints from the previous step), δ_{12}, and Λ (see *SI Appendix* for details).

The resulting polymer model captures the thermodynamics of complex formation, both in terms of the reaction enthalpy and free energy for different salt concentrations (Fig. 4G), as well as the salt concentration-dependent chain dimensions (Fig. 4F) with only four adjustable parameters, w_0, δ_0, δ_{12}, and Λ. In line with our simple estimate for a Gaussian chain above, the change in configurational entropy of the chains upon binding (ΔF_5, *SI Appendix*, Fig. S3) makes a negligible contribution to the total free energy. The total enthalpy is determined by the balance between the Coulomb energy of ion-pair formation (F_4) and the enthalpic part of the free energy from correlations between free ions (F_3). With increasing salt concentration, more counterions are released upon IDP complex formation (Fig. 4H), but the decreasing entropy gain of each released ion owing to the larger bulk salt concentration compensates this effect and moderates the overall entropic driving force from counterion release at high salt (*SI Appendix*, Fig. S3). The decrease in enthalpy as a function of salt concentration resulting from the reduction in the number of bound ion pairs is offset by the increase in energy gain from more pronounced correlations between the free ions at higher salt concentrations (*SI Appendix*, Fig. S3). By considering the effect of the local dielectric environment on the electrostatic energy of ion pair formation, it becomes apparent that the entropy gain from the released counterions (ΔF_2) is the primary thermodynamic driving force (*SI Appendix*, Fig. S3).

Discussion

Most high-affinity protein complexes involve enthalpic and entropic contributions that are both favorable (17, 35). The high-affinity disordered complex between H1 and ProTα stands in contrast to this behavior: Its binding is entropically driven, with a large unfavorable enthalpy of similar magnitude as the total free energy of complex formation. Our results suggest that counterion-release entropy is a strong driving force for PH complex formation. This finding highlights the importance of counterions in interactions involving highly charged biomacromolecules and leads to behavior such as increasing affinity with temperature (Figs. 1C and 4E). Polyelectrolyte interactions of this kind abound in the cell, especially in the nucleus, where charged IDPs and nucleic acids are key players in chromatin structure and transcriptional regulation (15, 28, 79–81).

Much of the behavior we observe here for H1 and ProTα is reminiscent of synthetic polyelectrolytes (36, 37, 41, 42, 82), especially the important role of counterion release entropy (42, 82) and the endothermic character of the interaction (36, 37). However, a key aspect of our results is that we unambiguously detect and quantify the presence of stoichiometrically defined soluble complexes between H1 and ProTα—the PH dimer and the two ternary
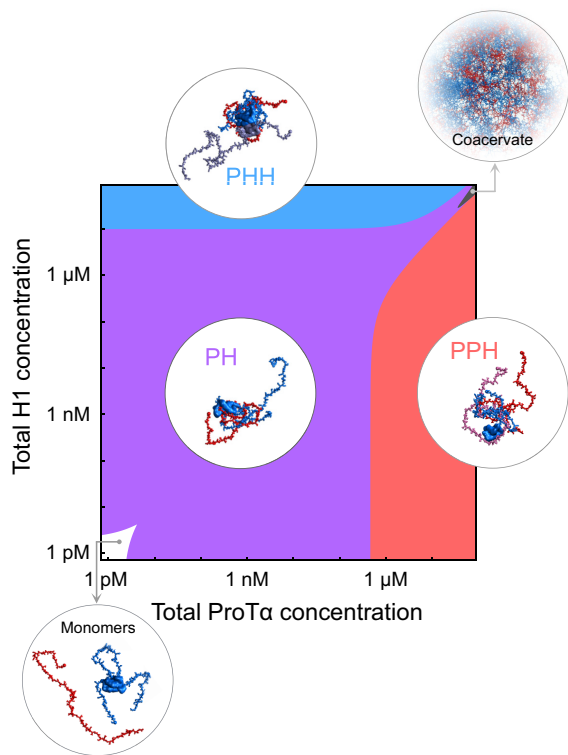
Fig. 5. Diagram of assembly states formed by H1 and ProTα as a function of protein concentrations at 165 mM monovalent salt. The colored regions indicate the predominant oligomeric species. If both protein concentrations are in the low picomolar range or below (white area), ProTα and H1 are predominantly monomeric. In the purple, blue, and red regions, ProTα-H1 (PH), ProTα-H1$_2$ (PHH), and ProTα$_2$-H1 (PPH) are the predominant oligomeric species, respectively. The dark gray region at high concentrations of both proteins indicates conditions where phase separation by complex coacervation occurs (57). Note that the re-entrant boundaries for complex coacervation are approximate. The other regions are calculated based on the equilibrium dissociation constants K_D^{PH}, K_D^{PPH}, and K_D^{PHH} at 165 mM salt (*SI Appendix*, Eqs. **S1**–**S3**). Snapshots of complexes and the dense phase are based on simulations (13, 59).

complexes PPH and PHH—afforded by the ability of single-molecule spectroscopy to identify different molecular species as distinct subpopulations (29–32). Only at near charge-balanced stoichiometry and above tens of micromolar protein concentrations does phase separation set in at physiological salt concentrations (Fig. 5) (60). For synthetic polyelectrolytes, as well as some biomolecular systems such as gelatin, indications for the presence of soluble complexes from experiments have been reported (36, 37, 83, 84), but the unambiguous detection and characterization of species such as dimeric and trimeric complexes has remained elusive, presumably owing to the low critical concentrations for the coacervation of binary mixtures of oppositely charged polyelectrolytes (21, 85) and the lack of experimental methods required for investigating the ultralow polyelectrolyte concentrations where the association equilibria for the formation of dimers and ternary complexes can be probed. Correspondingly, the formation of well-defined oligomeric polyelectrolyte complexes has primarily been investigated via simulations and theory (42, 57, 64, 65, 82, 86), and small soluble complexes such as dimers have been postulated to be a first step of polyelectrolyte complexation preceding coacervation (37, 83, 84, 87). Considering the obvious parallels between highly charged IDPs and synthetic polyelectrolytes, the dimers and ternary complexes of ProTα and H1 are thus likely to resemble the small soluble complexes of synthetic polyelectrolytes. Our single-molecule approach is expected to be extendable to synthetic polyelectrolytes and would facilitate their quantitative investigation, including their mechanistic role in coacervation.

Another parallel to the behavior of synthetic polyelectrolytes is the thermodynamic signature we observe for the formation of ProTα-H1 oligomers, especially its endothermicity, which requires a pronounced entropic driving force to yield a strong interaction. A positive interaction enthalpy has previously been reported for synthetic polyelectrolytes, but the need to separate the contributions of small oligomers from coacervation complicates quantitative modeling (36, 37). Here, we demonstrate that such modeling is feasible for H1 and ProTα since phase separation is absent under our experimental conditions, and independent information on the stabilities and thus concentrations of the contributing dimer and ternary complexes is available from single-molecule measurements. Obviously, both the dimer and the ternary complexes need to be accounted for in the quantitative analysis of binding experiments at micromolar protein concentrations, where they are substantially populated at physiologically relevant salt concentrations. This insight resolves the orders-of-magnitude discrepancy between the affinity of the PH complex obtained from single-molecule experiments and the apparent affinities inferred from ITC if an inadequate model involving only dimer formation is assumed (34). Ternary complex formation also reconciles the fast exchange between bound and unbound states observed in NMR experiments at high micromolar concentrations with the high affinity of ProTα-H1 complex formation (28). The underlying mechanism of competitive substitution (88) may also be involved in transcriptional regulation (15).

We rationalize our results with concepts from the field of synthetic polyelectrolytes (13, 28, 31, 36, 37, 42, 64, 65, 82, 83, 87), in particular a minimal mean-field theory that treats a salt-moderated balance between Coulomb energy of bound ion pairs and free-ion entropy, and accounts for counterion adsorption and release (64, 65). Recent theoretical considerations based on the temperature dependence of the relative permittivity of bulk water suggest the relevance of solvent entropy for polyelectrolyte interactions related to the reorientational entropy of the dipolar solvent associated with ion-pair formation (57). Our theoretical approach indicates substantial counterion condensation on the chains, potentially amplified by a reduced dielectric constant near the polypeptide chain (48, 89, 90), which is expected to render solvent orientation effects small compared to the entropy gain from counterion release. One way of testing and refining the parameters used in the current theoretical framework might be all-atom molecular dynamics simulations (60, 62, 91). The modular nature of the theory would in principle also allow aspects such as charge patterning and charge regulation (92, 93) to be incorporated explicitly.

Our results may further contribute to a quantitative understanding of polyelectrolyte complex coacervation by complementing theories for phase separation that explicitly account for polyelectrolyte-associated counterions (36, 94–96) but do not yet account for the diversity of soluble complexes in the dilute phase. From the perspective of kinetics (97), the formation of small oligomers or clusters may be the earliest steps of phase separation, and for subsaturated solutions of several RNA-binding proteins that undergo homotypic phase separation, a heterogeneous distribution of clusters ranging from tens or hundreds of molecules to mesoscale assemblies has been observed (98). A continuum of such assemblies may thus provide a link between the small oligomers we observe here and phase separation. However, in contrast to homotypic cluster formation, in heterotypic systems such as ProTα and H1, not only the absolute but also the relative concentrations are crucial for cluster formation. In such systems, higher-order oligomers may define the phase boundaries, particularly for reentrant phase separation (99). It will be an interesting topic of future research whether an analogous broad range of heterotypic oligomers and clusters exists for systems like H1 and ProTα that undergo complex coacervation.

With counterion release entropy as a principle driving force for polyelectrolyte complex formation, the affinity between chains can potentially become extremely large since the number of counterions adsorbed on a polyelectrolyte chain increases with the number of charged groups and thus the degree of polymerization (48, 64, 66). The cellular milieu is rife with highly charged flexible biopolymers, such as nucleic acids (100), inorganic polyphosphate (101), and highly charged IDPs (13), and high-affinity interactions as well as complex coacervation can result without the need for interactions encoded by folded domains. Considering the combinatorial possibilities of complexes that can arise from such polyelectrolyte molecules in a cell, an obvious question is the origin of specificity in such interactions. Specificity can arise from distinct patterns of spatial and temporal localizations and concentrations of interaction partners such that the likelihood of a specific pair of such molecules forming a complex is maximized. Other regulatory processes, such as posttranslational modifications, to which IDPs are particularly amenable, as well as patterning of charged residues, can also contribute (18, 102, 103). Polyelectrolyte interactions are likely to often act in synergy with structured domains and motifs, a combination that is widespread in nucleic acid-binding proteins (104). Polyelectrolyte interactions and counterion release as a driving force are thus likely to be of general importance for biomolecular interactions (19, 24, 51, 105), and understanding the underlying mechanisms will be essential for quantifying intracellular communication.

Material and Methods

Proteins were recombinantly expressed in *Escherichia coli*, purified, and labeled for single-molecule FRET experiments as described previously (13, 28, 77). The details of single-molecule experiments and the experimental setup have been described before (13, 28, 106). Calorimetry experiments were performed on a MicroCal iTC200 calorimeter. See *SI Appendix* for detailed descriptions on protein expression, purification, labeling, single-molecule FRET, and calorimetry experiments and analysis, and a description of the theory.

Data, Materials, and Software Availability. Code for analysis of single-molecule and computational data has been deposited in GitHub (https://github.com/SchulerLab/Fretica.git) (107). All other data are included in the manuscript and/or supporting information.

Author affiliations: ªDepartment of Biochemistry, University of Zurich, Zurich 8057, Switzerland; ᵇDepartment of Physical Sciences and Centre for Advanced Functional Materials, Indian Institute of Science Education and Research Kolkata, Mohanpur 741246, India; and ᶜDepartment of Physics, University of Zurich, Zurich 8057, Switzerland

1. V. Csizmok, A. V. Follis, R. W. Kriwacki, J. D. Forman-Kay, Dynamic protein interaction networks and new structural paradigms in signaling. *Chem. Rev.* **116**, 6424–6462 (2016).
2. R. B. Berlow, H. J. Dyson, P. E. Wright, Functional advantages of dynamic protein disorder. *FEBS Lett.* **589**, 2433–2440 (2015).
3. A. K. Dunker, M. S. Cortese, P. Romero, L. M. Iakoucheva, V. N. Uversky, Flexible nets. The roles of intrinsic disorder in protein interaction networks. *FEBS J.* **272**, 5129–5148 (2005).
4. P. E. Wright, H. J. Dyson, Linking folding and binding. *Curr. Opin. Struct. Biol.* **19**, 31–38 (2009).
5. P. Tompa, M. Fuxreiter, Fuzzy complexes: Polymorphism and structural disorder in protein-protein interactions. *Trends Biochem. Sci.* **33**, 2–8 (2008).
6. T. Mittag, L. E. Kay, J. D. Forman-Kay, Protein dynamics and conformational disorder in molecular recognition. *J. Mol. Recognit.* **23**, 105–116 (2010).
7. T. Mittag et al., Dynamic equilibrium engagement of a polyvalent ligand with a single-site receptor. *Proc. Natl. Acad. Sci. U.S.A.* **105**, 17772–17777 (2008).
8. S. Milles et al., Plasticity of an ultrafast interaction between nucleoporins and nuclear transport receptors. *Cell* **163**, 734–745 (2015).
9. B. Schuler et al., Binding without folding–the biomolecular function of disordered polyelectrolyte complexes. *Curr. Opin. Struct. Biol.* **60**, 66–76 (2020).
10. A. L. Turner et al., Highly disordered histone H1-DNA model complexes and their condensates. *Proc. Natl. Acad. Sci. U.S.A.* **115**, 11964–11969 (2018).
11. N. Danilenko et al., Histone chaperone exploits intrinsic disorder to switch acetylation specificity. *Nat. Commun.* **10**, 3435 (2019).
12. E. D. Holmstrom, Z. Liu, D. Nettels, R. B. Best, B. Schuler, Disordered RNA chaperones can enhance nucleic acid folding via local charge screening. *Nat. Commun.* **10**, 2453 (2019).
13. A. Borgia et al., Extreme disorder in an ultrahigh-affinity protein complex. *Nature* **555**, 61–66 (2018).
14. E. M. George, D. T. Brown, Prothymosin α is a component of a linker histone chaperone. *FEBS Lett.* **584**, 2833–2836 (2010).
15. P. O. Heidarsson et al., Release of linker histone from the nucleosome driven by polyelectrolyte competition with a disordered protein. *Nat. Chem.* **14**, 224–231 (2022).
16. S. L. Shammas, J. M. Rogers, S. A. Hill, J. Clarke, Slow, reversible, coupled folding and binding of the spectrin tetramerization domain. *Biophys. J.* **103**, 2203–2214 (2012).
17. W. E. Stites, Protein−protein interactions: Interface structure, binding thermodynamics, and mutational analysis. *Chem. Rev.* **97**, 1233–1250 (1997).
18. M. K. Hazra, Y. Levy, Affinity of disordered protein complexes is modulated by entropy–energy reinforcement. *Proc. Natl. Acad. Sci. U.S.A.* **119**, e2120456119 (2022).
19. M. Muthukumar, 50th anniversary perspective: A perspective on polyelectrolyte solutions. *Macromolecules* **50**, 9528–9560 (2017).
20. J. van der Gucht, E. Spruijt, M. Lemmers, M. A. Cohen Stuart, Polyelectrolyte complexes: Bulk phases and colloidal systems. *J. Colloid Interface Sci.* **361**, 407–422 (2011).
21. S. Srivastava, M. V. Tirrell, Polyelectrolyte complexation. *Adv. Chem. Phys.* **161**, 499–544 (2016).
22. V. A. Kabanov, Polyelectrolyte complexes in solution and in bulk. *Russ. Chem. Rev.* **74**, 3–20 (2005).
23. A. M. Rumyantsev, N. E. Jackson, J. J. de Pablo, Polyelectrolyte complex coacervates: Recent developments and new frontiers. *Annu. Rev. Condens. Matter Phys.* **12**, 155–176 (2021).
24. M. T. Record Jr., C. F. Anderson, T. M. Lohman, Thermodynamic analysis of ion effects on the binding and conformational equilibria of proteins and nucleic acids: The roles of ion association or release, screening, and ion effects on water activity. *Q. Rev. Biophys.* **11**, 103–178 (1978).
25. C. E. Sing, Development of the modern theory of polymeric complex coacervation. *Adv. Colloid Interface Sci.* **239**, 2–16 (2017).
26. K. Achazi et al., Understanding the interaction of polyelectrolyte architectures with proteins and biosystems. *Angew. Chem. Int. Ed. Engl.* **60**, 3882–3904 (2021).
27. C. L. Cooper, P. L. Dubin, A. B. Kayitmazer, S. Turksen, Polyelectrolyte–protein complexes. *Curr. Opin. Colloid Interface Sci.* **10**, 52–78 (2005).
28. A. Sottini et al., Polyelectrolyte interactions enable rapid association and dissociation in high-affinity disordered protein complexes. *Nat. Commun.* **11**, 5736 (2020).
29. A. C. Ferreon, C. R. Moran, Y. Gambin, A. A. Deniz, Single-molecule fluorescence studies of intrinsically disordered proteins. *Methods Enzymol.* **472**, 179–204 (2010).
30. L. A. Metskas, E. Rhoades, Single-molecule FRET of intrinsically disordered proteins. *Annu. Rev. Phys. Chem.* **71**, 391–414 (2020).
31. A. Chowdhury, D. Nettels, B. Schuler, Interaction dynamics of intrinsically disordered proteins from single-molecule spectroscopy. *Annu. Rev. Biophys.* **52**, 433–462 (2023).
32. H. Mazal, G. Haran, Single-molecule FRET methods to study the dynamics of proteins at work. *Curr. Opin. Biomed. Eng.* **12**, 8–17 (2019).
33. E. Sisamakis, A. Valeri, S. Kalinin, P. J. Rothwell, C. A. M. Seidel, Accurate single-molecule FRET studies using multiparameter fluorescence detection. *Methods Enzymol.* **475**, 455–514 (2010).
34. H. Feng, B. R. Zhou, Y. Bai, Binding affinity and function of the extremely disordered protein complex containing human linker histone H1.0 and its chaperone protalpha. *Biochemistry* **57**, 6645–6648 (2018).
35. J. A. Caro et al., Entropy in molecular recognition by proteins. *Proc. Natl. Acad. Sci. U.S.A.* **114**, 6563 (2017).
36. L.-W. Chang et al., Sequence and entropy-based control of complex coacervates. *Nat. Commun.* **8**, 1273 (2017).
37. D. Priftis, N. Laugel, M. Tirrell, Thermodynamic characterization of polypeptide complex coacervation. *Langmuir* **28**, 15947–15957 (2012).
38. B. I. M. Wicky, S. L. Shammas, J. Clarke, Affinity of IDPs to their targets is modulated by ion-specific changes in kinetics and residual structure. *Proc. Natl. Acad. Sci. U.S.A.* **114**, 9882–9887 (2017).
39. S. Müller-Späth et al., Charge interactions can dominate the dimensions of intrinsically disordered proteins. *Proc. Natl. Acad. Sci. U.S.A.* **107**, 14609–14614 (2010).
40. J. Lipfert, S. Doniach, R. Das, D. Herschlag, Understanding nucleic acid-ion interactions. *Annu. Rev. Biochem.* **83**, 813–841 (2014).
41. J. Fu, J. B. Schlenoff, Driving forces for oppositely charged polyion association in aqueous solutions: Enthalpic, entropic, but not electrostatic. *J. Am. Chem. Soc.* **138**, 980–990 (2016).
42. Z. Ou, M. Muthukumar, Entropy and enthalpy of polyelectrolyte complexation: Langevin dynamics simulations. *J. Chem. Phys.* **124**, 154902 (2006).

43. G. S. Manning, J. Ray, Counterion condensation revisited. *J. Biomol. Struct. Dyn.* **16**, 461–476 (1998).

44. R. Vancraenebroeck, Y. S. Harel, W. Zheng, H. Hofmann, Polymer effects modulate binding affinities in disordered proteins. *Proc. Natl. Acad. Sci. U.S.A.* **116**, 19506–19512 (2019).

45. A. G. Kozlov, T. M. Lohman, Effects of monovalent anions on a temperature-dependent heat capacity change for Escherichia coli SSB tetramer binding to single-stranded DNA. *Biochemistry* **45**, 5190–5205 (2006).

46. L. B. Overman, W. Bujalowski, T. M. Lohman, Equilibrium binding of Escherichia coli single-strand binding protein to single-stranded nucleic acids in the (SSB)65 binding mode. Cation and anion effects and polynucleotide specificity. *Biochemistry* **27**, 456–471 (1988).

47. K. A. Vander Meulen, R. M. Saecker, M. T. Record, Formation of a wrapped DNA–Protein interface: Experimental characterization and analysis of the large contributions of ions and water to the thermodynamics of binding IHF to H′ DNA. *J. Mol. Biol.* **377**, 9–27 (2008).

48. M. Muthukumar, Theory of counter-ion condensation on flexible polyelectrolytes: Adsorption mechanism. *J. Chem. Phys.* **120**, 9343–9350 (2004).

49. A. Tamura, P. L. Privalov, The entropy cost of protein association. *J. Mol. Biol.* **273**, 1048–1060 (1997).

50. P. L. Privalov, A. I. Dragan, C. Crane-Robinson, Interpreting protein/DNA interactions: Distinguishing specific from non-specific and electrostatic from non-electrostatic components. *Nucleic Acids Res.* **39**, 2483–2491 (2011).

51. M. T. Record Jr., W. Zhang, C. F. Anderson, Analysis of effects of salts and uncharged solutes on protein and nucleic acid equilibria and processes: A practical guide to recognizing and interpreting polyelectrolyte effects, Hofmeister effects, and osmotic effects of salts. *Adv. Protein Chem.* **51**, 281–353 (1998).

52. M. Heyden, Disassembling solvation free energies into local contributions-toward a microscopic understanding of solvation processes. *Wiley Interdiscip. Rev. Comput. Mol. Sci.* **9**, e1390 (2019).

53. M. M. Garner, D. C. Rau, Water release associated with specific binding of gal repressor. *EMBO J.* **14**, 1257–1263 (1995).

54. J.-H. Ha, M. W. Capp, M. D. Hohenwalter, M. Baskerville, M. T. Record, Thermodynamic stoichiometries of participation of water, cations and anions in specific and non-specific binding of lac repressor to DNA: Possible thermodynamic origins of the "glutamate effect" on protein-DNA interactions. *J. Mol. Biol.* **228**, 252–264 (1992).

55. M. G. Fried et al., Role of hydration in the binding of lac repressor to DNA. *J. Biol. Chem.* **277**, 50676–50682 (2002).

56. F. F. Theisen et al., Quantification of conformational entropy unravels effect of disordered flanking region in coupled folding and binding. *J. Am. Chem. Soc.* **143**, 14540–14550 (2021).

57. S. Chen, Z.-G. Wang, Driving force and pathway in polyelectrolyte complex coacervation. *Proc. Natl. Acad. Sci. U.S.A.* **119**, e2209975119 (2022).

58. T. Y. Chen, Y. S. Cheng, P. S. Huang, P. Chen, Facilitated unbinding via multivalency-enabled ternary complexes: New paradigm for protein-DNA interactions. *Acc. Chem. Res.* **51**, 860–868 (2018).

59. Y. Zhang et al., Molecular origin of the glass transition in polyelectrolyte assemblies. *ACS Cent. Sci.* **4**, 638–644 (2018).

60. N. Galvanetto et al., Extreme dynamics in a biomolecular condensate. *Nature* **619**, 876–883 (2023).

61. M. W. Freyer, E. A. Lewis, Isothermal titration calorimetry: Experimental design, data analysis, and probing macromolecule/ligand binding and kinetic interactions. *Methods Cell Biol.* **84**, 79–113 (2008).

62. M. J. Fossat, X. Zeng, R. V. Pappu, Uncovering differences in hydration free energies and structures for model compound mimics of charged side chains of amino acids. *J. Phys. Chem. B* **125**, 4148–4161 (2021).

63. A. Cooper, Heat capacity effects in protein folding and ligand binding: A re-evaluation of the role of water in biomolecular thermodynamics. *Biophys. Chem.* **115**, 89–97 (2005).

64. S. Ghosh, S. Mitra, A. Kundagrami, Polymer complexation: Partially ionizable asymmetric polyelectrolytes. *J. Chem. Phys.* **158**, 204903 (2023), 10.1063/1065.0147323.

65. S. Mitra, A. Kundagrami, Polyelectrolyte complexation of two oppositely charged symmetric polymers: A minimal theory. *J. Chem. Phys.* **158**, 014903 (2023).

66. A. Kundagrami, M. Muthukumar, Effective charge and coil—globule transition of a polyelectrolyte chain. *Macromolecules* **43**, 2574–2581 (2010).

67. S. F. Edwards, P. Singh, Size of a polymer molecule in solution. Part 1.–Excluded volume problem. *J. Chem. Soc. Faraday Trans.* **275**, 1001–1019 (1979).

68. M. Muthukumar, Adsorption of a polyelectrolyte chain to a charged surface. *J. Chem. Phys.* **86**, 7230–7235 (1987).

69. M. Muthukumar, *Physics of Charged Macromolecules: Synthetic and Biological Systems* (Cambridge University Press, Cambridge, 2023).

70. R. K. Das, R. V. Pappu, Conformations of intrinsically disordered proteins are influenced by linear sequence distributions of oppositely charged residues. *Proc. Natl. Acad. Sci. U.S.A.* **110**, 13392–13397 (2013).

71. M. A. S. Hass, F. A. A. Mulder, Contemporary NMR studies of protein electrostatics. *Annu. Rev. Biophys.* **44**, 53–75 (2015).

72. M. J. Fossat, A. E. Posey, R. V. Pappu, Quantifying charge state heterogeneity for proteins with multiple ionizable residues. *Biophys. J.* **120**, 5438–5453 (2021).

73. R. Kjellander, A multiple decay-length extension of the Debye-Hückel theory: To achieve high accuracy also for concentrated solutions and explain under-screening in dilute symmetric electrolytes. *Phys. Chem. Chem. Phys.* **22**, 23952–23985 (2020).

74. B. J. Payliss, J. Vogel, A. K. Mittermaier, Side chain electrostatic interactions and pH-dependent expansion of the intrinsically disordered, highly acidic carboxyl-terminus of γ-tubulin. *Protein Sci.* **28**, 1095–1105 (2019).

75. K. Tamiola, R. M. Scheek, P. van der Meulen, F. A. A. Mulder, pepKalc: Scalable and comprehensive calculation of electrostatic interactions in random coil polypeptides. *Bioinformatics* **34**, 2053–2060 (2018).

76. R. Wuttke et al., Temperature-dependent solvation modulates the dimensions of disordered proteins. *Proc. Natl. Acad. Sci. U.S.A.* **111**, 5213–5218 (2014).

77. A. Chowdhury et al., Mechanism-dependent modulation of ultrafast interfacial water dynamics in intrinsically disordered protein complexes. *Angew. Chem. Int. Ed. Engl.* **58**, 4720–4724 (2019).

78. E. Fischermeier et al., Dipolar relaxation dynamics at the active site of an ATPase regulated by membrane lateral pressure. *Angew. Chem. Int. Ed. Engl.* **56**, 1269–1272 (2017).

79. B. Schuler et al., Binding without folding–the biomolecular function of disordered polyelectrolyte complexes. *Curr. Opin. Struct. Biol.* **60**, 66–76 (2019).

80. C. F. Anderson, M. T. Record Jr., Salt-nucleic acid interactions. *Annu. Rev. Phys. Chem.* **46**, 657–700 (1995).

81. J. Liu et al., Intrinsic disorder in transcription factors. *Biochemistry* **45**, 6873–6888 (2006).

82. V. S. Rathee, H. Sidky, B. J. Sikora, J. K. Whitmer, Role of associative charging in the entropy-energy balance of polyelectrolyte complexes. *J. Am. Chem. Soc.* **140**, 15319–15328 (2018).

83. L. Vitorazi et al., Evidence of a two-step process and pathway dependency in the thermodynamics of poly(diallyldimethylammonium chloride)/poly(sodium acrylate) complexation. *Soft Matter.* **10**, 9496–9505 (2014).

84. A. Veis, A review of the early development of the thermodynamics of the complex coacervation phase separation. *Adv. Colloid Interface Sci.* **167**, 2–11 (2011).

85. E. Spruijt, A. H. Westphal, J. W. Borst, M. A. Cohen Stuart, J. van der Gucht, Binodal compositions of polyelectrolyte complexes. *Macromolecules* **43**, 6476–6484 (2010).

86. E. Meneses-Juárez, C. Márquez-Beltrán, J. F. Rivas-Silva, U. Pal, M. González-Melchor, The structure and interaction mechanism of a polyelectrolyte complex: A dissipative particle dynamics study. *Soft Matter* **11**, 5889–5897 (2015).

87. S. Chen, P. Zhang, Z.-G. Wang, Complexation between oppositely charged polyelectrolytes in dilute solution: Effects of charge asymmetry. *Macromolecules* **55**, 3898–3909 (2022).

88. B. Peng, M. Muthukumar, Modeling competitive substitution in a polyelectrolyte complex. *J. Chem. Phys.* **143**, 243133 (2015).

89. E. L. Mehler, G. Eichele, Electrostatic effects in water-accessible regions of proteins. *Biochemistry* **23**, 3887–3891 (1984).

90. G. Lamm, G. R. Pack, Calculation of dielectric constants near polyelectrolytes in solution. *J. Phys. Chem. B* **101**, 959–965 (1997).

91. G. M. Wadsworth et al., RNAs undergo phase transitions with lower critical solution temperatures. bioRxiv [Preprint] (2022). https://doi.org/10.1101/2022.10.17.512593 (Accessed 14 September 2023).

92. L. Sawle, K. Ghosh, A theoretical method to compute sequence dependent configurational properties in charged polymers and proteins. *J. Chem. Phys.* **143**, 085101 (2015).

93. M. Ghasemi, R. G. Larson, Role of electrostatic interactions in charge regulation of weakly dissociating polyacids. *Prog. Polym. Sci.* **112**, 101322 (2021).

94. S. Adhikari, M. A. Leaf, M. Muthukumar, Polyelectrolyte complex coacervation by electrostatic dipolar interactions. *J. Chem. Phys.* **149**, 163308 (2018).

95. A. Salehi, R. G. Larson, A molecular thermodynamic model of complexation in mixtures of oppositely charged polyelectrolytes with explicit account of charge association/dissociation. *Macromolecules* **49**, 9706–9719 (2016).

96. T. K. Lytle, C. E. Sing, Transfer matrix theory of polymer complex coacervation. *Soft Matter* **13**, 7001–7012 (2017).

97. E. W. Martin et al., A multi-step nucleation process determines the kinetics of prion-like domain phase separation. *Nat. Commun.* **12**, 4513 (2021).

98. M. Kar et al., Phase-separating RNA-binding proteins form heterogeneous distributions of clusters in subsaturated solutions. *Proc. Natl. Acad. Sci. U.S.A.* **119**, e2202222119 (2022).

99. A. N. Milin, A. A. Deniz, Reentrant phase transitions and non-equilibrium dynamics in membraneless organelles. *Biochemistry* **57**, 2470–2477 (2018).

100. A. Plumridge, S. P. Meisburger, L. Pollack, Visualizing single-stranded nucleic acids in solution. *Nucleic Acids Res.* **45**, e66 (2017).

101. K. D. Kumble, A. Kornberg, Inorganic polyphosphate in mammalian cells and tissues. *J. Biol. Chem.* **270**, 5818–5822 (1995).

102. A. H. Phillips, R. W. Kriwacki, Intrinsic protein disorder and protein modifications in the processing of biological signals. *Curr. Opin. Struct. Biol.* **60**, 1–6 (2020).

103. C. W. Pak et al., Sequence determinants of intracellular phase separation by complex coacervation of a disordered protein. *Mol. Cell* **63**, 72–85 (2016).

104. H. J. Dyson, Roles of intrinsic disorder in protein–nucleic acid interactions. *Mol. Biosyst.* **8**, 97–104 (2012).

105. N. Korolev, A. Allahverdi, A. P. Lyubartsev, L. Nordenskiold, The polyelectrolyte properties of chromatin. *Soft Matter* **8**, 9322–9333 (2012).

106. D. Nettels et al., Single molecule spectroscopy of the temperature-induced collapse of unfolded proteins. *Proc. Natl. Acad. Sci. U.S.A.* **106**, 20740–20745 (2009).

107. D. Nettels, B. Schuler, Fretica. GitHub. https://github.com/SchulerLab/Fretica.git. Accessed 17 September 2023.

108. K.-I. Tainaka, Effect of counterions on complex coacervation. *Biopolymers* **19**, 1289–1298 (1980).

109. D. Priftis, M. Tirrell, Phase behaviour and complex coacervation of aqueous polypeptide solutions. *Soft Matter* **8**, 9396–9405 (2012).

110. R. Chollakup, W. Smitthipong, C. D. Eisenbach, M. Tirrell, Phase behavior and coacervation of aqueous poly(acrylic acid)—poly(allylamine) solutions. *Macromolecules* **43**, 2518–2528 (2010).

111. A. Salehi, P. S. Desai, J. Li, C. A. Steele, R. G. Larson, Relationship between polyelectrolyte bulk complexation and kinetics of their layer-by-layer assembly. *Macromolecules* **48**, 400–409 (2015).

112. T. Farhat, G. Yassin, S. T. Dubas, J. B. Schlenoff, Water and ion pairing in polyelectrolyte multilayers. *Langmuir* **15**, 6621–6623 (1999).

113. J. R. Vieregg et al., Oligonucleotide-peptide complexes: Phase control by hybridization. *J. Am. Chem. Soc.* **140**, 1632–1638 (2018).

114. P. Schaaf, J. B. Schlenoff, Saloplastics: Processing compact polyelectrolyte complexes. *Adv. Mater.* **27**, 2420–2432 (2015).

115. Q. Wang, J. B. Schlenoff, The polyelectrolyte complex/coacervate continuum. *Macromolecules* **47**, 3108–3116 (2014).

116. S. Meng, J. M. Ting, H. Wu, M. V. Tirrell, Solid-to-liquid phase transition in polyelectrolyte complexes. *Macromolecules* **53**, 7944–7953 (2020).

117. S. L. Perry et al., Chirality-selected phase behaviour in ionic polypeptide complexes. *Nat. Commun.* **6**, 6052 (2015).

118. A. Vidyasagar, C. Sung, R. Gamble, J. L. Lutkenhaus, Thermal transitions in dry and hydrated layer-by-layer assemblies exhibiting linear and exponential growth. *ACS Nano* **6**, 6174–6184 (2012).

119. Y. Chen, M. Yang, J. B. Schlenoff, Glass transitions in hydrated polyelectrolyte complexes. *Macromolecules* **54**, 3822–3831 (2021).

PNAS

Supporting Information for
Driving forces of the complex formation between highly charged disordered proteins

Aritra Chowdhury[1], Alessandro Borgia[1,2], Souradeep Ghosh[3], Andrea Sottini[1], Soumik Mitra[3], Rohan Eapen[1], Madeleine B. Borgia[1,2], Tianjin Yang[1], Nicola Galvanetto[1,4], Miloš T. Ivanović[1], Pawel Lukijanczuk[1], Ruijing Zhu[1], Daniel Nettels[1], Arindam Kundagrami[3], Benjamin Schuler[1,4]

[1]Department of Biochemistry, University of Zurich, Zurich, 8057 Switzerland

[2]Current Address: Department of Structural Biology, St. Jude Children's Research Hospital, Memphis, TN 38105, USA

[3]Department of Physical Sciences and Centre for Advanced Functional Materials, Indian Institute of Science Education and Research Kolkata, Mohanpur 741246, India

[4]Department of Physics, University of Zurich, Zurich, 8057 Switzerland

Email: a.chowdhury@bioc.uzh.ch, arindam@iiserkol.ac.in, schuler@bioc.uzh.ch

This PDF file includes:

Supporting Text
Figures S1 to S5
Tables S1 to S4
SI References

Supporting Text

Protein preparation and labeling

Recombinant human histone H1.0 produced in *E. coli* was from New England Biolabs (cat. # M2501S). Unlabeled ProTα (WT isoform 2) and ProTα 56C/110C (isoform 1), used for fluorescent labeling, were purified using His$_6$-tagged constructs as described previously[1-4]. ProTα 2C/110C (isoform 1) used for fluorescent labeling was either expressed and purified as a His$_6$-tagged construct as described previously or was cloned into a pBAD-IntCBD-12His vector and purified according to a previously described protocol[5]. Note that although His$_6$- or His$_{12}$-tags were used for purification by immobilized metal chelate affinity chromatography, the tags were subsequently removed in all cases by protease cleavage or thiol-induced self-cleavage of an intein[5] for His$_6$- and His$_{12}$-bearing proteins, respectively. See Table S3 for all protein sequences used in the measurements. For fluorescence labeling, 10-15 nmol of the purified protein were reduced with 10 mM Tris(2-carboxyethyl) phosphine hydrochloride (TCEP) for one hour in phosphate-buffered saline (PBS), pH 7, supplemented with 4 M guanidinium chloride (GdmCl) and 0.2 mM EDTA. Excess TCEP was removed subsequently via repeated (5x) buffer exchange using 3-kDa molecular weight cut off centrifugal concentrators with the labeling buffer (PBS pH 7, 4 M GdmCl, 0.2 mM TCEP and 0.2 mM EDTA). The protein was subsequently labeled with Alexa488-C5 maleimide and Alexa594-C5 maleimide (Invitrogen) using ~6.5-fold molar excess of both the dyes relative to protein at room temperature for one hour followed by overnight incubation at 4 °C. The unreacted dye was quenched with 10 mM dithiothreitol at room temperature for 10 minutes and removed subsequently by repeated buffer exchange with labeling buffer using centrifugal concentrators. The double-labeled protein was separated from the reaction mixture by RP-HPLC on a Reprosil Gold C18 column (Dr. Maisch, Germany), lyophilized, and stored at −80 °C. The integrity of all the samples was confirmed using electrospray ionization mass spectrometry.

Single-molecule spectroscopy

Single-molecule FRET experiments were performed on freely diffusing molecules with a MicroTime 200 confocal single-molecule instrument (PicoQuant, Berlin, Germany). The samples were excited with a 488-nm laser (Sapphire 488–100 CDRH, Coherent, Santa Clara, CA) through a high-numerical aperture water-immersion objective (Olympus UplanApo 60x/1.20 W). The fluorescence signal was spatially filtered using a 100-μm pinhole and split into donor and acceptor signals using a dichroic mirror (585DCXR, Chroma, Rockingham, VT); each component, after further spectral filtering using bandpass filters (Chroma ET525/50 M for donor signal and HQ650/100 for acceptor signal), was focused on an avalanche photodiode detector (SPCM-AQR-15, PerkinElmer Optoelectronics, Vaudreuil, QC, Canada). A HydraHarp 400 (PicoQuant, Berlin, Germany) was used to record individual photon arrival times from the detectors. Most experiments were performed with continuous-wave laser excitation. Temperature-dependent experiments were performed with pulsed interleaved excitation (PIE)[6], where the samples were excited with alternating pulses of the 488-nm laser and laser emission at 585 nm, obtained by spectrally filtering the output of a supercontinuum laser (EX-12 SuperK Extreme, NKT photonics); laser synchronization for PIE experiments was achieved with a Sepia II laser driver (PicoQuant, Berlin, Germany). All experiments were performed with 50-100 pM doubly labeled samples in 10 mM Tris buffer (pH 7.4), containing different concentrations of salts and sometimes additional additives, as stated in main text, supplemented with 0.01% Tween 20 to prevent surface adhesion of molecules and 140 mM β-mercaptoethanol as a photoprotectant. All experiments, except temperature-dependent measurements, were performed in chambered plastic cover slides (μ-Slide, ibidi, Germany) to minimize protein surface adhesion.

For temperature-dependent experiments, a custom-built sample holder allowing temperature control with a water-cooled Peltier element driven by a temperature controller (BelektroniG, Germany) was used[7]; the objective was heated and cooled with an aluminum collar containing a Peltier element driven by a temperature controller (BelektroniG, Germany). A glass cuvette was used for temperature measurements[7]. To prevent surface adhesion of protein molecules, the glass surface was coated with the amorphous fluoropolymer CYTOP (CTX-809AP2, solvent CT-SOLV180, AGC Chemicals Europe, Thornton-Cleveleys, United Kingdom)[8]. The cylinder and the bottom glass coverslip of the cuvette were first cleaned by boiling with 2% Deconex® INSTRUMENT PLUS (Borer Chemie AG, Zuchwil, Switzerland) solution and double-distilled water, and subsequently plasma-oxidized (Femto 1A, Diener electronic, Ebhausen, Germany) for 60 seconds at 25% power. The surfaces of the glass cylinder and the coverslip were modified with (3-aminopropyl)-triethoxysilane (APTES, Sigma-Aldrich, Buchs, Switzerland) with a 5% v/v ethanolic APTES solution for 30 minutes. Unreacted APTES was removed by rinsing the cylinder and the coverslip with ethanol followed by drying with compressed air. The glass slide was spin-coated with CYTOP solution (9% w/v) at 900 rpm, achieving a coating thickness of ~4 µm. The cylinder was dip-coated in the CYTOP solution (9% w/v). Afterwards, the cylinder and glass slide were placed on a hot plate set to 70 °C for 30 minutes to let the solvent evaporate. Finally, the cylinder and the coverslip were aligned and thermally bonded for 2 hours at 180 °C, above the glass transition temperature of CYTOP. For some temperature-dependent experiments, a customized 3D-printed cuvette using a photoreactive poly-urethane resin (UltraCur3D RG35 from BASF, Germany) was used, with comparable results. The temperature in the confocal volume was calibrated via the temperature-dependent fluorescence lifetime of Rhodamine B[7,9].

From the fluorescence recordings of freely diffusing single molecules, transfer efficiencies from the selected photon bursts (≥3000 bursts for each measurement), each originating from a single molecule traversing the confocal volume, were quantified according to $E = n_A/(n_D + n_A)$, where n_D and n_A are the numbers of donor and acceptor photons, respectively, following donor excitation in a given burst, corrected for background, spectral crosstalk between channels, acceptor direct excitation, and differences in dye quantum yields and detection efficiencies[10]. For PIE experiments, stoichiometry ratios were additionally calculated from every burst according to $S = (n_D + n_A)/(n_D + n_A + n_A^A)$, where n_A^A is the number acceptor photons following acceptor excitation in a given burst, corrected for background signal and different donor and acceptor laser excitation intensities[10]. Data analysis was performed with Fretica, a custom add-on for Mathematica (Wolfram Research) available at https://github.com/SchulerLab.

Binding affinity from single-molecule experiments

We employed single-molecule FRET using double-labeled ProTα (P*) to measure the dissociation constants K_D^{PH}, K_D^{PPH}, and K_D^{PHH} for the following equilibria:

$$P + H \underset{}{\overset{K_D^{PH}}{\rightleftharpoons}} PH \qquad\qquad \text{eq.1}$$

$$PH + P \underset{}{\overset{K_D^{PPH}}{\rightleftharpoons}} PPH \qquad\qquad \text{eq.2}$$

$$PH + H \underset{}{\overset{K_D^{PHH}}{\rightleftharpoons}} PHH \qquad\qquad \text{eq.3}$$

For measuring K_D^{PH}, we titrated 50-70 pM P* with increasing amounts of unlabeled H1, and the series of transfer efficiency histograms was fitted globally with a sum of two Gaussian peak functions of independent amplitudes but shared positions and widths among the histograms.

The areas of the two peaks are proportional to the concentrations, c_{P^*H} and c_{P^*}, of bound and unbound P*, respectively, allowing us to quantify the fraction of heterodimer, $\theta_{PH} = \frac{c_{P^*H}}{c_{P^*}+c_{P^*H}}$, as a function of the total H1 concentration added, c_H^{tot}. Fitting these measured fractions with

$$\theta_{PH}(c_H^{tot}) = \frac{\left(c_H^{tot} + K_D^{PH} + c_{P^*}^{tot}\right) - \sqrt{\left(c_H^{tot} + K_D^{PH} + c_{P^*}^{tot}\right)^2 - 4c_H^{tot}c_{P^*}^{tot}}}{2c_{P^*}^{tot}}, \qquad \text{eq.4}$$

where $c_{P^*}^{tot}$ is the known total P* concentration, yields K_D^{PH}. For temperature-dependent measurements, the bound fraction was measured for a given concentration of H1 at different temperatures, and the temperature-dependent values of K_D^{PH} were obtained by solving eq. 4 for K_D^{PH}. At very low salt concentrations and in presence of osmolytes, eq. 4 was insufficient for fitting the binding isotherms owing to surface adhesion of H1, so in those cases, we applied a model that accounts for the competition between ProTα binding and surface adhesion of H1.[2]

K_D^{PHH} was estimated in a similar way as K_D^{PH}: We formed P*H by mixing 50-70 pM P* with 3 nM unlabeled H1, a concentration much greater than K_D^{PH} at the monovalent salt concentrations where these measurements were performed (~8-80 mM), and titrated the sample with increasing amounts of unlabeled H1. The resulting series of transfer efficiency histograms with two peaks corresponding to P*H and P*HH, were globally fitted as described above. From the relative areas under the peaks, we obtain the fraction $\theta_{PHH} = \frac{c_{P^*HH}}{c_{P^*H}+c_{P^*HH}}$ as a function of the excess H1 concentration, c_H^{ex}, which is given by the difference between total H1 concentration added, c_H^{tot}, and the initial P*H concentration, $c_{P^*H}^{ini}$. At the monovalent salt concentrations used, K_D^{PH} is sub-picomolar, and PH is fully formed, with negligible concentrations of unbound P* remaining, thus we assume $c_{P^*H}^{ini} = c_{P^*}^{tot}$ (the total P* concentration). Since $c_H^{tot} \gg c_{P^*H}^{ini}$, we assume $c_H^{ex} \approx c_H^{tot}$, and fitting the measured fractions with

$$\theta_{PHH}(c_H^{tot}) = \frac{\left(c_H^{tot} + K_D^{PHH} + c_{P^*H}^{ini}\right) - \sqrt{\left(c_H^{ex} + K_D^{PHH} + c_{P^*H}^{ini}\right)^2 - 4c_H^{ex}c_{P^*H}^{ini}}}{2c_{P^*H}^{ini}} \qquad \text{eq.5}$$

yields K_D^{PHH}.

K_D^{PPH} was estimated via a competition experiment where 10 nM unlabeled ProTα and H1 (P and H, respectively) doped with 50 pM P* were titrated with increasing concentrations of P at low monovalent salt concentration (~65-110 mM). Since the affinities of labeled and unlabeled ProTα for H1 are very similar[1], we assume that P* partitions equally into all ProTα-containing species and represents their relative equilibrium populations. The resulting series of transfer efficiency histograms were globally fitted as above, but now with a sum of three Gaussian peak functions for P*, P*H, and P*PH; the areas of the peaks are proportional to their respective concentrations, c_{P^*}, c_{P^*H}, and c_{P^*PH}, allowing us to quantify the fraction $\theta_{PPH} = \frac{c_{P^*PH}}{c_{P^*PH}+c_{P^*H}}$ as a function of the excess ProTα concentration, c_P^{ex}, which is the difference between the total ProTα concentration, c_P^{tot}, and the initial PH concentration, c_{PH}^{ini}. At the low salt concentrations used, K_D^{PH} is sub-picomolar, PH is fully formed, and its initial concentration, c_{PH}^{ini}, is thus equal to 10 nM. Fitting the measured fractions with

$$\theta_{PPH}(c_P^{ex}) = \frac{\left(c_P^{ex} + K_D^{PPH} + c_{PH}^{ini}\right) - \sqrt{\left(c_P^{ex} + K_D^{PPH} + c_{PH}^{ini}\right)^2 - 4c_P^{ex}c_{PH}^{ini}}}{2c_{PH}^{ini}}, \qquad \text{eq.6}$$

yields $K_{\mathrm{D}}^{\mathrm{PPH}}$. For all affinities measured by single-molecule FRET, we conservatively quote an error of a factor 2 in K_{D} (corresponding to ±0.7 k_{B}T in binding free energy), based on the variance previously observed for K_{D} measurements from repeat experiments and the variance of different dye pairs and labeling positions[1]. We note that ProTα by itself remains monomeric up to a concentration of at least 5 mg/mL according to scattering experiments[11].

ProTα dimensions and associated configurational entropy change estimated from single-molecule FRET

Single-molecule FRET of the terminally labeled (2C/110C) variant of ProTα was used to estimate average root-mean-square (RMS) end-to-end distances. Transfer efficiency histograms measured at different concentrations of KCl and in the absence and presence of H1 were fitted with a Gaussian peak function to estimate the corresponding mean transfer efficiencies $\langle E \rangle$, from which the RMS distances were inferred using the relation

$$\langle E \rangle = \int_0^\infty P(r)E(r)dr \,, \tag{eq.7}$$

where $P(r)$ is a distance probability density function, and $E(r)$ is given by

$$E(r) = R_0^6/(R_0^6 + r_0^6) \,, \tag{eq.8}$$

where the Förster radius R_0 is 5.4 nm for Alexa 488 and 594 in water and was corrected for the refractive index of the solution (using the known dependence of refractive index on KCl concentration)[12]. We used the empirically modified self-avoiding random walk model (SAW-v) for $P(r)$[13]. The length scaling exponent, v, was obtained for the 2-110 segment of ProTα by accounting for the total length of both linkers and fluorophores equivalent to 9 amino acids[14]. Finally, the average end-to-end distance of the entire ProTα chain (R_e) was estimated using the value of v obtained and the number of peptide bonds (110 for ProTα). We approximate the change in free energy due to the change in configurational entropy of ProTα upon binding H1, ΔG_{conf}, by assuming $P(r)$ for a Gaussian chain, as

$$\frac{\Delta G_{conf}}{k_{\mathrm{B}}T} = \ln \frac{R_{e,u}}{R_{e,b}} \,, \tag{eq.9}$$

where $R_{e,u}$ and $R_{e,b}$ are the average root-mean-square end-to-end distances for unbound and H1-bound ProTα, respectively[15].

Salt and osmolyte dependences of H1-ProTα binding

In the presence of a salt of monovalent cations and anions, n_- anions (A^-) and n_+ cations (C^+) associated with the individual proteins are released upon H1-ProTα binding[16]:

$$\mathrm{ProTα} + \mathrm{H1} \rightleftharpoons \mathrm{ProTα}\text{-}\mathrm{H1} + n_+C^+ + n_-A^-. \tag{eq.10}$$
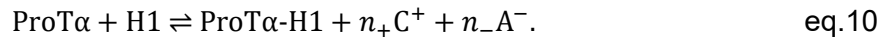
For binding in the presence of a salt of monovalent cations and divalent anions (A^{2-}), we have:

$$\mathrm{ProTα} + \mathrm{H1} \rightleftharpoons \mathrm{ProTα}\text{-}\mathrm{H1} + n_+C^+ + n_{2-}A^{2-}, \tag{eq.11}$$
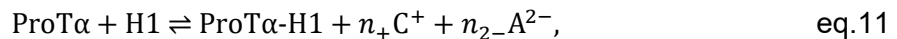
and in the presence of a salt of monovalent anions and divalent cations (C^{2+}),

$$\mathrm{ProTα} + \mathrm{H1} \rightleftharpoons \mathrm{ProTα}\text{-}\mathrm{H1} + n_{2+}C^{2+} + n_-A^- , \tag{eq.12}$$
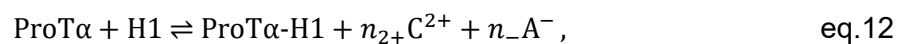
where n_{2+} and n_{2-} denote the numbers of released divalent cations and anions, respectively.

One can relate the dependence of the observed equilibrium dissociation constant for H1-ProTα binding, $K_{\mathrm{D}}^{\mathrm{PH}}$, as a function of the mean ionic activity of a given salt to the number of ions released upon H1 binding to ProTα[2,16]. The respective relations for different salts, either

with monovalent cations and anions (LiCl, KCl, CsCl), with divalent cation and monovalent anion (MgCl$_2$), and with monovalent cation and divalent anions (K$_2$SO$_4$) are given by

$$n_+ + n_- = n_{\text{mono}} = \frac{d \log K_D^{\text{PH}}}{d \log a_\pm} \qquad \text{eq.13}$$

$$n_{2+} + n_- = n_{\text{di-cat}} = \frac{d \log K_D^{\text{PH}}}{d \log a_\pm} \qquad \text{eq.14}$$

$$n_+ + n_{2-} = n_{\text{di-an}} = \frac{d \log K_D^{\text{PH}}}{d \log a_\pm}, \qquad \text{eq.15}$$

where $a_\pm$ is the mean ionic activity calculated as described below (eq. 16). If we assume that the number of charges released upon H1-ProTα binding is independent of the type of salt used, and that an equal number of positive and negative charges are released, i.e., $n_+ = n_-$, $n_{2+} = \frac{1}{2}n_+$, and $n_{2-} = \frac{1}{2}n_-$, we obtain $n_{\text{di-cat}} = n_{\text{di-an}} = 0.75\, n_{\text{mono}}$. The dependence of K_D^{PH} on mean ionic activity for the different salts was analyzed globally using eqs. (13-15) after substituting $n_{\text{di-cat}}$ and $n_{\text{di-an}}$ with $0.75\, n_{\text{mono}}$ in eqs. (14-15), with n_{mono} as a shared parameter for all data sets.

The mean ionic activity, $a_\pm$, for a molal concentration, m, of a salt is given by

$$a_\pm = m_\pm \gamma_\pm, \qquad \text{eq.16}$$

where $m_\pm$ is the mean ionic molality given by $m_\pm = m \left(v_+^{v_+} v_-^{v_-}\right)^{\frac{1}{(v_+ + v_-)}}$; v_+ and v_- are the stoichiometric coefficients of the cation and the anion, respectively; and $\gamma_\pm$ is the mean ionic activity coefficient[17]. The tabulated concentration dependences of $\gamma_\pm$ for the different salts[12] were interpolated with empirical equations (See Table S4 and Fig. S5) to obtain values of $a_\pm$ for all salt concentrations used. Note that at the low salt concentrations we used, molar and molal concentrations are virtually indistinguishable, and hence the former was used as a proxy for the latter.

The water activity, a_w, was varied with the neutral osmolyte triethylene glycol[18] (over a range of ~5-15% v/v) and quantified by vapor pressure osmometry (Vapro, ELITechGroup, France). a_w is related to the measured osmolality, m_s, by[19]

$$a_w = \exp(-m_s M_w), \qquad \text{eq.17}$$

where M_w is the molar mass of pure water.

Isothermal titration calorimetry (ITC)

ITC experiments were performed with a MicroCal iTC200 calorimeter (Malvern, UK) in 10 mM Tris buffer (pH 7.4) containing different concentrations of potassium chloride to attain different monovalent salt concentrations. For every salt concentration, two titrations were performed: H1 (H) was titrated with ProTα (P) and *vice versa*. A ~250-µM stock solution of the proteins was dialyzed against 150 mL of the measurement buffer overnight to equilibrate the samples with the same buffer. For the titrations, the titrand concentration in the ITC cell was kept between 15 and 25 µM, and the titrant concentration in the syringe was between 150 and 250 µM. To estimate the sample concentration loss due to surface adhesion, the titrant concentration was measured in the unused solution in the syringe after completion of the experiment, and the titrand concentration was measured before starting the titration by aspirating excess solution from the sample cell after cell loading was complete. Protein concentrations were measured spectrophotometrically on a Nanodrop (Thermo Scientific),

using an extinction coefficient of 3840 M⁻¹cm⁻¹ at 280 nm for H1 and extinction coefficients of 89,508 and 33,636 M⁻¹cm⁻¹ for ProTα at 215 nm and 225 nm, respectively[11].

Since ITC experiments are conducted in overfill mode, there is a volume displacement with every injection of the titrant that has to be accounted for to obtain accurate titrant and titrand concentrations in the cell, c_t and c_d, respectively, at any point of the injection sequence[20,21]:

$$c_{\mathrm{d}} = c_{\mathrm{d}}^0 \left(\frac{2V_0 - \Delta V}{2V_0 + \Delta V} \right) \qquad \text{eq.18}$$

$$c_{\mathrm{t}} = c_{\mathrm{t}}^0 \left(\frac{2\Delta V}{\Delta V + 2V_0} \right), \qquad \text{eq.19}$$

where c_{d}^0 is the initial titrand concentration in the cell, c_{t}^0 is the initial titrant concentration in the syringe, V_0 is the cell volume, and ΔV is the total displaced volume after n injections, $\Delta V = \sum_{i=1}^{n} V_i$, where V_i is the volume of the ith injection. Complexation between P and H involves the three binding equilibria given by eqs. 1-3, associated with the molar enthalpy changes ΔH^{PH}, ΔH^{PPH}, and ΔH^{PHH}, respectively. The total heat absorbed cumulatively by the solution relative to unbound P and H after the ith injection is

$$Q(i) = V_0 \left[c_{\mathrm{PH}} \Delta H^{\mathrm{PH}} + c_{\mathrm{PPH}} \left(\Delta H^{\mathrm{PH}} + \Delta H^{\mathrm{PPH}} \right) + c_{\mathrm{PHH}} \left(\Delta H^{\mathrm{PH}} + \Delta H^{\mathrm{PHH}} \right) \right], \qquad \text{eq.20}$$

where c_{PH}, c_{PPH}, and c_{PHH} are the concentrations of PH, PPH, and PHH, respectively, in the cell after the ith injection. The reaction heat of the ith injection, $\Delta Q(i)$, normalized by the molar amount of titrant injected, Δn_t, is given by

$$\frac{\Delta Q(i)}{\Delta n_t} = \frac{Q(i) - Q(i-1) + \frac{V_i}{V_0} \left(\frac{Q(i) + Q(i-1)}{2} \right)}{c_{\mathrm{t}}^0 V_i}, \qquad \text{eq.21}$$

where V_i is the volume of the ith injection[21]. To calculate the ITC thermograms, we first calculated c_{PH}, c_{PPH}, and c_{PHH} for given total concentrations of P, $c_{\mathrm{P}}^{\mathrm{tot}}$, and H, $c_{\mathrm{H}}^{\mathrm{tot}}$, by solving the system of eqs. 22-26 numerically

$$K_{\mathrm{D}}^{\mathrm{PH}} = \frac{c_{\mathrm{P}} c_{\mathrm{H}}}{c_{\mathrm{PH}}} \qquad \text{eq.22}$$

$$K_{\mathrm{D}}^{\mathrm{PPH}} = \frac{c_{\mathrm{PH}} c_{\mathrm{P}}}{c_{\mathrm{PPH}}} \qquad \text{eq.23}$$

$$K_{\mathrm{D}}^{\mathrm{PHH}} = \frac{c_{\mathrm{PH}} c_{\mathrm{H}}}{c_{\mathrm{PHH}}} \qquad \text{eq.24}$$

$$c_{\mathrm{P}}^{\mathrm{tot}} = c_{\mathrm{P}} + c_{\mathrm{PH}} + 2c_{\mathrm{PPH}} + c_{\mathrm{PHH}} \qquad \text{eq.25}$$

$$c_{\mathrm{H}}^{\mathrm{tot}} = c_{\mathrm{H}} + c_{\mathrm{PH}} + c_{\mathrm{PPH}} + 2c_{\mathrm{PHH}} \qquad \text{eq.26}$$

with respect to c_P, c_H, c_{PH}, c_{PPH}, and c_{PHH} for given values of $K_{\mathrm{D}}^{\mathrm{PH}}$, $K_{\mathrm{D}}^{\mathrm{PPH}}$, $K_{\mathrm{D}}^{\mathrm{PHH}}$, $c_{\mathrm{P}}^{\mathrm{tot}}$, and $c_{\mathrm{H}}^{\mathrm{tot}}$. c_P and c_H are the concentrations of free P and H, respectively. The result allowed us to calculate the thermograms using eqs. 18-21. The calculated $\frac{\Delta Q(i)}{\Delta n}$ values were fitted to the experimental ones by minimizing the residual sum of squares using a Nelder-Mead simplex algorithm in Mathematica (Wolfram Research). ΔH^{PH}, ΔH^{PPH}, ΔH^{PHH}, $K_{\mathrm{D}}^{\mathrm{PH}}$, $K_{\mathrm{D}}^{\mathrm{PPH}}$, $K_{\mathrm{D}}^{\mathrm{PHH}}$ are adjustable parameters for minimization. We allow for a ±20% uncertainty on titrant and titrand concentrations (instead of an uncertainty on stoichiometry) and for an offset between experimental and calculated $\frac{\Delta Q(i)}{\Delta n}$ to correct for non-specific heats[22,23]. The binding free energies were constrained to within an interval of ±1.5 $k_{\mathrm{B}}T$ of the values extrapolated from the

single-molecule measurements (Fig. S2) to account for the uncertainty of these values; the offset between the experimental and the calculated $\frac{\Delta Q(i)}{\Delta n}$ values was constrained to within an interval of ±3 kcal mol^{-1} (±12.6 kJ mol^{-1}), and the heat evolved for the last injection was subtracted from the thermograms before quantifying $\frac{\Delta Q(i)}{\Delta n}$ values. To fit the thermograms with a two-state binding model involving only the binding equilibrium given by eq. 1, the analogous approach was used, but with

$$Q(i) = \frac{V_0 \, \Delta H^{\mathrm{PH}}}{2} \left[c_{\mathrm{H}}^{\mathrm{tot}} + c_{\mathrm{P}}^{\mathrm{tot}} + K_{\mathrm{D}}^{\mathrm{PH}} - \sqrt{(c_{\mathrm{P}}^{\mathrm{tot}} - c_{\mathrm{H}}^{\mathrm{tot}})^2 - 2(c_{\mathrm{P}}^{\mathrm{tot}} + c_{\mathrm{H}}^{\mathrm{tot}})K_{\mathrm{D}}^{\mathrm{PH}} + (K_{\mathrm{D}}^{\mathrm{PH}})^2} \right] \quad \text{eq.27}$$

instead of eq. 20. Subsequently, as in the previous case, the calculated $\frac{\Delta Q(i)}{\Delta n}$ values were fitted to experimental ones by minimizing the residual sum of squares with ΔH^{PH} and $K_{\mathrm{D}}^{\mathrm{PH}}$ as adjustable parameters, allowing for a 20% error on titrant and titrand concentrations, and an offset between the experimental and calculated $\frac{\Delta Q(i)}{\Delta n}$. For the enthalpies from the thermogram fits, we use a conservative estimate of the uncertainty of ±20% of the resulting values, given that we allow for a 20% error on titrant and titrand concentrations.

Analysis of the temperature-dependent ProTα-H1 affinity with single-molecule FRET

The temperature dependence of $K_{\mathrm{D}}^{\mathrm{PH}}$ from the single-molecule FRET measurements at different salt concentrations was fitted with the integrated form of the Van 't Hoff equation[24],

$$ln \frac{K_{\mathrm{D}}^{\mathrm{PH}}(T_0)}{K_{\mathrm{D}}^{\mathrm{PH}}(T)} = \frac{\Delta H^{\mathrm{PH}}(T_0) - T_0 \Delta C_{\mathrm{p}}}{R} \left(\frac{1}{T_0} - \frac{1}{T} \right) + \frac{\Delta C_{\mathrm{p}}}{R} ln \frac{T}{T_0}, \quad \text{eq.28}$$

where R is the universal gas constant, $K_{\mathrm{D}}^{\mathrm{PH}}(T)$ is the equilibrium dissociation constant at absolute temperature T; $\Delta H^{\mathrm{PH}}(T_0)$ and $K_{\mathrm{D}}^{\mathrm{PH}}(T_0)$ are the corresponding values at the reference temperature T_0, and ΔC_{p} is the change in heat capacity upon binding. Using $\Delta H^{\mathrm{PH}}(T_0)$, with T_0 = 276K, directly from the ITC measurements or from a linear interpolation of ΔH^{PH} as a function of salt concentration, we fitted all data sets globally with ΔC_{p} as a shared fit parameter.

Theory for complexation between two flexible polyelectrolytes

<u>Free energy of two oppositely charged partially ionized interacting IDPs of different lengths</u>

The theoretical framework we adapt here for complex formation between H1 and ProTα was previously described[25,26] and is based on the Edwards Hamiltonian[27] extended by Muthukumar for Coulomb interactions[28-30]; hence we provide only a short summary and mention the required modifications here. A dilute solution of volume Ω contains the two oppositely charged IDPs (ProTα and H1), which are modeled as flexible polyions[25,26,29,31] with their respective counterions and added salt. The polyions have different lengths and are partially ionized (only a fraction of the monomers are charged), with the ionizable monomers uniformly distributed along the chains[26]. The polyanion (PA) and polycation (PC) consist of N_1 and N_2 monomers, respectively, of which N_{c1} and N_{c2} are ionizable, respectively. There are N_{c1} and N_{c2} countercations and counteranions, respectively, that make the system electroneutral. All charges are assumed to be monovalent. At any time during the complexation process between the two chains, let n be the number of ionizable PA monomers, as well as PC monomers, that form the intermediate complex, which is thus taken to be electroneutral. The complexation process continues until all ionizable PA monomers are neutralized by PC monomers (for our purpose, the PA is assumed to contain fewer ionizable monomers than the PC, i.e. $N_{c1} < N_{c2}$, and consequently $n = N_{c1}$. The maximum degree of ionization is $f_{mi} = N_{ci}/N_i$, where i = 1, 2

indicate the PA and the PC, respectively, implying that $n_i = n/f_{mi}$ is the total number of monomers in the intermediate complex from the ith chain.

In the intermediate state, M_i out of N_{ci} counterions remain condensed on the uncomplexed parts of the PA and PC, so the degrees of ionization of the uncomplexed parts are $f_i = (N_i f_{mi} - M_i - n)/(N_i - (n/f_{mi}))$. Let c_s be the number density of an added monovalent salt that dissociates into n_+ cations and n_- anions, where $c_s = n_+/\Omega = n_-/\Omega \equiv n_s/\Omega$. Therefore, $N_{ci} - M_i + n_s$ $(i = 1, 2)$ cations and anions, respectively, remain free in solution. The degree of counterion condensation for the uncomplexed chain parts is defined by $\alpha_i' = M_i/(N_i - (n/f_{mi}))$, which gives $f_i = f_{mi} - \alpha_i'$. The degree of ionization of the entire polyion (including both the complexed and uncomplexed parts) may be defined as $f_{Ti} = f_{mi} - M_i/N_i - n/N_i$, with the corresponding set of new variables related to α_i', which are $\alpha_i = M_i/(f_{mi}N_i - n) = \alpha_i'/f_{mi}$.

We consider the total free energy of the system[25,26] with the intermediate complex of n mutually bound, ionizable monomer pairs and $n_i(= n/f_{mi})$ total (ionizable as well as neutral) monomers from each polyion i, the counterions, and the implicit solvent. For each of the uncomplexed chain parts, M_i counterions are distributed within a volume for which the outer boundary is a cylinder of radius $d_c = \ell/4 + r_c$, and the inner boundary is set by the segment length along the chain (Fig. S3A), where ℓ is the Kuhn length, and r_c is the counterion diameter. The cylinder radius is set so that a counterion on the chain contour can be accommodated; thus, although $\ell/4$ seems counterintuitive as opposed to $\ell/2$, this discrepancy arises from the difference between the Kuhn length and segment length, necessitating a renormalization of the degree of polymerization and the effective length scale (see the following section). The translational entropy of counterions condensed on the polyions leads to the free energy contribution

$$\frac{F_1}{k_B T} = \sum_{i=1}^{2} \bar{\Omega}_{ci} \left[\left(1 - \frac{M_i}{\bar{\Omega}_{ci}}\right) \log\left(1 - \frac{M_i}{\bar{\Omega}_{ci}}\right) + \frac{M_i}{\bar{\Omega}_{ci}} \log\left(\frac{M_i}{\bar{\Omega}_{ci}}\right) \right], \qquad \text{eq.29}$$

where the rescaled dimensionless volume of the cylinder is $\bar{\Omega}_{ci} = (N_i - n_i)\left(\pi \tilde{d}_c^2 - 1/4\right)/\tilde{r}_c^3$, and $\tilde{r}_c$ and $\tilde{d}_c$ are the rescaled dimensionless ionic size parameter and the rescaled dimensionless diameter of the cylinder, respectively, given by $\tilde{r}_c = r_c/\ell$ and $\tilde{d}_c = d_c/\ell$.

Considering $N_i f_{mi} - M_i + n_s$ free ions of species i, the free energy contribution from the translational entropy of ions free in solution takes the form

$$\frac{F_2}{k_B T} = \sum_{i=1}^{2} N_i \left[\left\{ \left(f_{mi} - \frac{n}{N_i}\right)(1 - \alpha_i) + \frac{n}{N_i} + \frac{\bar{c}_s}{\bar{\rho}_i} \right\} \log\left(\bar{\rho}_i \left(f_{mi} - \frac{n}{N_i}\right)(1 - \alpha_i) + \frac{\bar{\rho}_i n}{N_i} + \bar{c}_s\right) \right.$$
$$\left. - \left\{ \left(f_{mi} - \frac{n}{N_i}\right)(1 - \alpha_i) + \frac{n}{N_i} + \frac{\bar{c}_s}{\bar{\rho}_i} \right\} \right], \qquad \text{eq.30}$$

where $\bar{\rho}_i = N_i/(\Omega/r_c^3)$ and $\bar{c}_s = n_s/(\Omega/r_c^3)$.

The free-energy contribution from the correlations between all dissociated counterions is given by

$$\frac{F_3}{k_B T} = -\Lambda \frac{\tilde{\kappa}^3 \tilde{r}_c^3}{12\pi} \frac{N_i}{\bar{\rho}_i}, \qquad \text{eq.31}$$

where the Λ is an empirical correction parameter[32] (see the following subsection for details), and the inverse Debye length, κ, is defined as

$$\tilde{\kappa}^2 = 4\pi \frac{\tilde{\ell}_B}{\tilde{r}_c^3} \left[\sum_{i=1}^{2} \bar{\rho}_i \left(f_{mi} - \frac{n}{N_i} \right) (1 - \alpha_i) + \frac{\bar{\rho}_i n}{N_i} + \bar{c}_s \right], \qquad \text{eq.32}$$

with $\tilde{\kappa} = \kappa \ell$.

Including all ion pairs (monomer-counterion and oppositely charged monomers) for the complexed and the uncomplexed chain parts, the electrostatic free energy of these ion pairs is

$$\frac{F_4}{k_B T} = -\sum_{i=1}^{2} \tilde{\ell}_B \delta_i N_i \left\{ \left(f_{mi} - \frac{n}{N_i} \right) - \left(1 - \frac{n_i}{N_i} \right) \right\} - n \tilde{\ell}_B \delta_{12}, \qquad \text{eq.33}$$

where $\delta_i = (\epsilon \ell / \epsilon_{li} d_{mc})$ are the dielectric 'mismatch' parameters for monomer-counterion pairing in the uncomplexed chain parts, d_{mc} is the dipole length of monomer-counterion pair, $\delta_{12} = \epsilon \ell / \epsilon_{l12} d_{mm}$ is the corresponding parameter for monomer-monomer pairing in the complexed part, and d_{mm} is the dipole length of monomer-monomer pairs. δ_i is a mean field parameter that accounts for microscopic aspects of ion pairing, and is thus simultaneously influenced by the difference between the local dielectric constants, ϵ_{li}, and the bulk dielectric constant of the medium, ϵ, as well as the effective dipole length for ion pairing. It should, however, be noted that the theory cannot provide separate estimates of the underlying microscopic parameters, i.e., the local dielectric constant and the effective dipole length.

The configurational and interaction free energy for two complexing polyions, originating from the Edwards-Muthukumar Hamiltonian[27-29], is variationally extremized[26]. The Hamiltonian is based upon an effective expansion factor ℓ_{1i} for R_{ei} of chain i with $R_{ei}^2 = N_i \ell \ell_{1i} \equiv N \ell^2 \tilde{\ell}_{1i} = 6 \tilde{R}_{gi}^2 \ell^2$, with $\tilde{\ell}_{1i} (= \ell_{1i}/\ell)$ and $\tilde{R}_{gi} = \frac{R_{gi}}{\ell}$ (R_{gi} is the radius of gyration of chain i) being the rescaled expansion factor and radius of gyration of chain i, respectively. Finally, using a Gaussian monomer distribution[26,33], the free-energy contribution due to the elastic entropy, self-interaction (both electrostatic and non-electrostatic) of the individual polyions, and the mutual interaction (both electrostatic and non-electrostatic) between the polyions is obtained as

$$\frac{F_5}{k_B T} = \frac{3}{2} \sum_{i=1}^{2} \left(\tilde{\ell}_{1i} - 1 - \log \tilde{\ell}_{1i} \right) + \left(\frac{9}{2\pi} \right)^{3/2} \sum_{i=1}^{2} \frac{w_{ii} N_i^{1/2}}{\tilde{\ell}_{1i}^{3/2}} + w_{12} N_1 N_2 \left(\frac{3}{4\pi \tilde{R}_{g0}^2} \right)^{3/2} \exp \left(-\frac{3 \tilde{R}^2}{4 \tilde{R}_{g0}^2} \right)$$
$$+ \sum_{i=1}^{2} \frac{f_i^2 (N_i - n_i)^2 \tilde{\ell}_B}{2} \Theta_s(\tilde{\kappa}, a_i) - f_1 f_2 (N_1 - n_1)(N_2 - n_2) \tilde{\ell}_B \Theta_m(\tilde{\kappa}, \tilde{R}, a_{12}), \qquad \text{eq.34}$$

where w_{ii} and w_{12} are the self- and inter-chain two-body non-electrostatic (excluded volume) interaction strengths, respectively, $\tilde{R} = |r_1 - r_2|/\ell = \tilde{R}_{g1} + \tilde{R}_{g2}$, $\tilde{R}_{g0}^2 = \sum_{i=1}^{2} \tilde{R}_{gi}^2$, with r_1 and r_2 being the centers of mass of the two chains, and

$$\Theta_s(\tilde{\kappa}, a_i) = \frac{2}{\pi} \left[\sqrt{\frac{\pi \tilde{\kappa}^2}{4 a_i}} - \frac{\tilde{\kappa} \pi}{2} \exp(a_i) \operatorname{erfc}(\sqrt{a_i}) \right], \qquad \text{eq.35}$$

where $a_i = \tilde{\kappa}^2 \tilde{R}_{gi}^2 (N_i - n_i)/3 N_i$, and $\Theta_m(\tilde{\kappa}, \tilde{R}, a_{12})$ is

$$\Theta_m(\tilde{\kappa}, \tilde{R}, a_{12}) = \frac{e^{a_{12}}}{\tilde{R}} \left[e^{-\tilde{\kappa} \tilde{R}} \operatorname{erfc} \left(\sqrt{a_{12}} - \frac{\tilde{\kappa} \tilde{R}}{2 \sqrt{a_{12}}} \right) - e^{\tilde{\kappa} \tilde{R}} \operatorname{erfc} \left(\sqrt{a_{12}} + \frac{\tilde{\kappa} \tilde{R}}{2 \sqrt{a_{12}}} \right) \right], \qquad \text{eq.36}$$

where $a_{12} = \sum_{i=1}^{2} \tilde{\kappa}^2 \tilde{R}_{gi}^2 (N_i - n_i)/6 N_i$.

Due to the differences in size and/or charge density of the chains, the total free energy, $F_1 + F_2 + F_3 + F_4 + F_5$ (eqs. 29-31 & 33-34), is minimized with respect to four variables, $f_{T1}, f_{T2}, \tilde{\ell}_{11}$, and $\tilde{\ell}_{12}$, using the Nelder-Mead simplex algorithm, using four adjustable parameters $\delta_0 (= \delta_1 = \delta_2), \delta_{12}, w_0 (= w_1 = w_2 = w_{12})$, and Λ, while r_c is fixed (see the section on parameterization). The free energy was originally constructed[26] for generic values of the overlap parameter n, and ideally, the dangling and complexed parts of each polyion had to be considered as two different chains with different size scaling (given by a single size expansion factor ℓ_1). In the present problem, however, only configurations of fully isolated ($n = 0$) and fully complexed ($n = N_{c1}$) polyions are of interest, for which the entire polyion can be assumed to have the same size scaling.

<u>Free energy of a single partially ionized flexible polyelectrolyte</u>

We use measurements of ProTα and H1 in isolation for defining the single-chain parameters of the theory[26,29] (see below) and thus also require the expression for the free energy of a single, isolated polyelectrolyte chain. The parameters for the various free energy components, F_1 to F_5, are analogous to the ones for two-chain complexation, and the single-chain expression can be obtained from eqs. 29-31 & 33-34 by setting $n = 0$, choosing the expression for one of the chains (removing the index i), and removing terms involving mutual interaction between the polyions ($\delta_{12}, w_{12}, f_1 f_2$ terms):

$$\frac{F_1}{k_B T} = \bar{\Omega}_c \left[\left(1 - \frac{M}{\bar{\Omega}_c} \right) \log \left(1 - \frac{M}{\bar{\Omega}_c} \right) + \left(\frac{M}{\bar{\Omega}_c} \right) \log \left(\frac{M}{\bar{\Omega}_c} \right) \right], \qquad \text{eq.37}$$

where $\bar{\Omega}_c = \frac{N}{\tilde{r}_c^3} \left(\pi \tilde{d}_c^2 - 1/4 \right)$.

$$\frac{F_2}{k_B T} = N \left\{ (f\bar{\rho} + \bar{c}_s) \log \left(f + \frac{\bar{c}_s}{\bar{\rho}} \right) + \frac{\bar{c}_s}{\bar{\rho}} \log \bar{c}_s - (f\bar{\rho} + \bar{c}_s) \right\} \qquad \text{eq.38}$$

$$\frac{F_3}{k_B T} = -\Lambda \frac{\Omega \kappa^3}{12\pi} = -\Lambda \frac{N\sqrt{4\pi\tilde{\ell}_B}}{3\bar{\rho}}^{3/2} (f\bar{\rho} + \bar{c}_s)^{3/2} = -\Lambda \frac{(\tilde{\kappa}\tilde{r}_c)^3}{12\pi}, \qquad \text{eq.39}$$

where $\tilde{\kappa} = \sqrt{\frac{4\pi\tilde{\ell}_B}{\tilde{r}_c^3} (\bar{\rho} f + \bar{c}_s)}$.

$$\frac{F_4}{k_B T} = -(1 - f) N \delta \tilde{\ell}_B \qquad \text{eq.40}$$

As before, N is the number of monomers in the chain, f the degree of ionization, $\bar{\rho}$ the rescaled monomer density, $\bar{c}_s$ the rescaled salt concentration, and κ the inverse Debye length. The dielectric mismatch parameter is $\delta = (\epsilon\ell/\epsilon_l d)$, with ϵ_l being the local dielectric constant, and d the dipole length of monomer-counter ion pairs. The configurational free energy of the chain is obtained by the variational method[26,28], in which one starts from the Edwards-Muthukumar Hamiltonian, considering uniform swelling of the chain with spherical symmetry,

$$\frac{F_5}{k_B T} = \frac{3}{2} \left[\tilde{\ell}_1 - 1 - \log \tilde{\ell}_1 \right] + \left(\frac{9}{2\pi} \right)^{3/2} w\sqrt{N} \frac{1}{\tilde{\ell}_1^{3/2}} + 2\sqrt{\frac{6}{\pi}} f^2 \tilde{\ell}_B \frac{N^{3/2}}{\tilde{\ell}_1^{1/2}} \Theta_0(\tilde{\kappa}, a), \qquad \text{eq.41}$$

where $\tilde{\ell}_1$ is the size expansion factor of the chain, and

$$\Theta_0(\tilde{\kappa}, a) = \frac{2}{\pi} \left[\sqrt{\frac{\pi\tilde{\kappa}^2}{4a}} - \frac{\tilde{\kappa}\pi}{2} \exp(a) \, \text{erfc}(\sqrt{a}) \right], \qquad \text{eq.42}$$

with $a \equiv \tilde{\kappa}^2 N \tilde{\ell}_1 / 6$, where a Gaussian monomer distribution for the chain has been used[26,33].

<u>Correction for the electrostatic free energy contribution due to the correlations between free ions at high salt concentrations</u>

The bare Debye-Hückel term in F_3 (eqs. 31 & 39) is insufficient for quantitatively describing the free energy at high salt concentrations (for $\kappa^{-1} \leq \ell_B$), so we invoke the empirical parameter Λ as a correction factor to obtain reasonable agreement with the experimental observables[32]. To this end, we turn to the starting point of the Debye-Hückel formalism, which is based on solving the Poisson-Boltzmann (PB) equation for the charge density of the ionic species in solution and the necessary approximation of linearizing the PB equation for low salt concentration, hence for small κ. This approach leads to $F_3/k_B T \simeq -\Omega \kappa^3/12\pi$.[34] At high salt, the linearization of the PB equation breaks down, and furthermore, the ionic atmosphere moving around the ion remains no longer symmetrical with respect to the charge distribution of the surrounding ions. These effects modify the electrostatic screening length and lead to multiple screening lengths distinct from that of the usual uniform Debye screening length κ^{-1}.[32]

Due to the presence of multiple electrostatic decay lengths, the modified mean electrostatic potential experienced by an ion q_j, $\psi_i^{\text{high}}(r)$, at high salt can be written as a perturbation sum over all possible decay lengths, of the form

$$
\begin{aligned}
\psi_i^{\text{high}}(r) \quad &= \frac{q_i^{\text{eff}_1}}{4\pi\epsilon_r^{\text{eff}_1}\epsilon_0} \frac{e^{-\kappa_1 r}}{r} + \frac{q_i^{\text{eff}_2}}{4\pi\epsilon_r^{\text{eff}_2}\epsilon_0} \frac{e^{-\kappa_2 r}}{r} + \cdots \\
&\simeq \frac{\Lambda q_i^{\text{eff}}}{4\pi\epsilon_r\epsilon_0} \frac{e^{-\kappa r}}{r} \\
&= \Lambda\psi_i(r)\,,
\end{aligned}
\qquad \text{eq.43}
$$

where κ_1, κ_2, etc. are the electrostatic decay lengths, and $q_i^{\text{eff}_1}$, $q_i^{\text{eff}_2}$, etc. are the effective charges as experienced by q_j, and $\epsilon_r^{\text{eff}_1}$, $\epsilon_r^{\text{eff}_2}$ represent the effective dielectric permittivity values (different from the solvent permittivity, ϵ_r) in the non-uniform ionic atmosphere. The effect of asymmetry in the charge distribution and the associated change in dielectric permittivity is collapsed into a single correction factor, Λ, with the potential form being kept invariant with respect to the bare Debye-Hückel term with a single decay length. Λ remains a multiplicative scalar upon integrating $\psi_i(r)$ to obtain the total electrostatic potential, and hence the free energy (eqs. 31 & 39)[34]. Ideally, Λ should be salt concentration-dependent; however, given that we apply the theory at moderately high salt concentrations across a relatively narrow concentration range, Λ was treated as a salt-invariant fit parameter for both the single-chain dimensions and the components of the free energy of complexation, and chosen by optimizing the agreement of the theory with the salt dependence of the free energy of chain complexation observed experimentally. Λ introduces minor modifications to the enthalpy of complexation (see Fig. S3B), whereas the major contribution comes from the entropy of the condensed and released ions and from the electrostatic free energy of condensed ions.

We estimate a release of ~45-60 counterions from the theory (depending on salt concentration), as opposed to ~18 estimated from the salt-dependent free energy of chain complexation using the Record-Lohmann framework[2,16]. Accounting for salt concentration-dependent ionic correlations significantly alters the entropy and enthalpy of counterion adsorption and release and consequently the thermodynamics of chain complexation; specifically, the number of counterions released is salt concentration-dependent. These aspects are not considered in the Record-Lohman framework and are the likely origin of the difference in estimates of counterion release from the two approaches. In other words, a larger number of counterions can actually be released upon chain complexation than would be

suggested from a Record-Lohman analysis of the salt dependence of the free energy or entropy.

<u>Parameterization of the system and numerical optimization of the parameters</u>

Upon eliminating the excluded volume and screened Coulomb interaction terms from the free energy of a single, isolated polyion, one recovers the theta-state dimensions of the chain given by $R_e = \sqrt{N}l$, where N and l are the number of segments and the segment length, respectively. The $C_\alpha - C_\alpha$ distance is 0.38 nm, but the theta-state dimensions for generic IDPs have been observed to be well approximated by $R_e = 0.55$ nm $\sqrt{N}$;[10,35] the increase in the effective segment length for the theta state from 0.38 nm to 0.55 nm is likely to be caused by local chain stiffness[36]. However, the contour length, L, is given by 0.38 nm N, and thus using 0.55 nm as a segment length would result in physically unrealistic chain dimensions. We thus rescale both N and l to obtain the rescaled parameters N' and l' by solving $N'l' = 0.38$ nm N and $\sqrt{N'}l' = 0.55$ nm $\sqrt{N}$, which yields $l' = 0.8$ nm and $N' = 0.48N$. With the rescaled parameters, we essentially obtain a projection of a generic IDP theta state on a Gaussian chain and recover both the theta state and the contour length. For ProTα, N' is 53. For H1, we approximated the contour as a 130-residue long IDP by replacing the folded domain with an effective chain segment of 10 peptide bonds (10 peptide bonds with a length scaling exponent of 0.63, representative of an expanded chain, matches the $C_\alpha - C_\alpha$ distance between the first and last structurally resolved residues of the globular domain; note that the exact choice of the scaling exponent minimally affects the length of the chain segment replacing the folded domain). This approach renders H1 amenable to investigation with our theory and is unlikely to strongly affect the interpretation, given that the globular domain contributes minimally to the overall dimensions, net-charge and binding affinity of H1 for ProTα[2]. The resulting value of N' we used for H1 is 62. For further parameterization, we used the measured chain dimensions of ProTα as described above, and for the same salt concentrations, the H1 chain dimensions were approximated by those of a chain with the same length scaling exponent experimentally obtained for ProTα and 129 peptide bonds.

The strength of the excluded volume interaction of the individual chains, w, can be obtained from the experimental single-chain dimensions at high salt concentration (Fig. S1) based on the configurational free energy of a single polyelectrolyte chain (eq. 41). With vanishing charge interactions (since at high salt concentrations, electrostatic interactions are effectively screened), the effective free energy at high salt takes the form:

$$\frac{F_5}{k_B T} = \frac{3}{2}\left[\tilde{\ell}_1 - 1 - \log \tilde{\ell}_1\right] + \left(\frac{9}{2\pi}\right)^{3/2} w\sqrt{N}\frac{1}{\tilde{\ell}_1^{3/2}}, \qquad \text{eq.44}$$

which upon minimization leads to a crossover relation for the chain expansion factor, $\tilde{\ell}_1$, as a function of w,

$$\tilde{\ell}_1^{5/2} - \tilde{\ell}_1^{3/2} = \left(\frac{9}{2\pi}\right)^{3/2} w\sqrt{N}, \qquad \text{eq.45}$$

which can be used to obtain the initial estimates for w to match the theoretical R_e of the chain with the experimentally obtained R_e at high salt concentration.

The rescaled ion size parameter, $\tilde{r}_c$, was set to 0.3; in terms of single-chain dimensions, for a given value of δ, the exact value of $\tilde{r}_c$ is virtually inconsequential within the range $1 \geq \tilde{r}_c > 0$, that is, for ion sizes smaller than the monomer length. In view of the low sensitivity of the result to variations in the excluded-volume parameters for ProTα-H1 complexation — which may not be surprising given the dominance of electrostatic interactions in such a highly charged system — we used a single excluded volume parameter, w_0 ($w_0 =$

$w_1 = w_2 = w_{12}$), for all non-electrostatic inter- and intra-chain interactions, and we estimated its value based on the dimensions of ProTα and H1 at high salt concentrations (above ~0.5 M; Fig. S4C) using eq. (45). We also used a single dielectric mismatch value δ_0 ($\delta_0 = \delta_1 = \delta_2$) for chain-counterion interactions, and we estimated bounds on δ_0 from the chain dimensions of ProTα and H1 and its experimental uncertainty at the lowest salt concentration using eqs. (37-41) and setting w_0 to the value obtained in the first step. In the next step, with w_0 fixed from the value obtained in the first step and δ_0 constrained to the bounds estimated form the previous step, we obtained values for δ_0, δ_{12}, and Λ by minimizing, based on a grid search, the residual sum of squares between experimental and computed free energy and enthalpy values associated with chain complexation, as a function of salt concentration using eqs. (29-34). To account for the different number of data points from chain complexation enthalpy (calorimetry) and chain complexation free energy (single-molecule FRET), the residual sums of squares were divided by the respective number of data points in the minimization. With the resulting parameter values, both the thermodynamic data (Fig. 4G) and the chain dimensions (Fig. 4F) as a function of salt concentration are described well by the theory.

<u>Assessing the potential effect of charge regulation</u>

To obtain an estimate of the contribution of charge regulation, we used the approach developed by Mulder and co-workers for unfolded and disordered proteins[37], building on site-specific information on protonation equilibria from NMR[38] and implemented in the pepKalc server[37]. Calculations for the ProTα sequence with pepKalc indicate that the structural charge (the charge at a given pH assuming unshifted canonical pK_a values for ionizable sidechains) of ProTα is recovered above ~100 mM salt (see Fig. S4). Furthermore, pH-dependent NMR experiments of the highly acidic C-terminal tubulin tail (NCPR of 0.34 vs. 0.40 for ProTα) also indicate that the net charge at neutral pH equals the structural charge in the presence of ~100 mM NaCl[39], in agreement with the pepKalc results on this protein. These results suggest that at salt concentrations where we measure H1-ProTα heterodimer formation, the salt concentration is high enough to suppress charge regulation. However, at low salt concentrations, the effect is significant and is therefore likely to affect our estimates of chain dimensions. To test this aspect, we estimated the chain dimensions for ProTα using eqs. 37-41 with the values of w_0 and δ_0 from Table S5, but setting the charge of ProTα to the value estimated from pepKalc at each salt concentration. The difference in dimensions using a nominal charge of -44 and using the charges from pepKalc is small compared to the relatively large experimental error (owing to the low transfer efficiencies observed in this range, Fig. S4). We note that this is an approximate approach; more precise effects of charge regulation would require a self-consistent theoretical framework including counterion condensation, charge regulation, and chain dimensions.
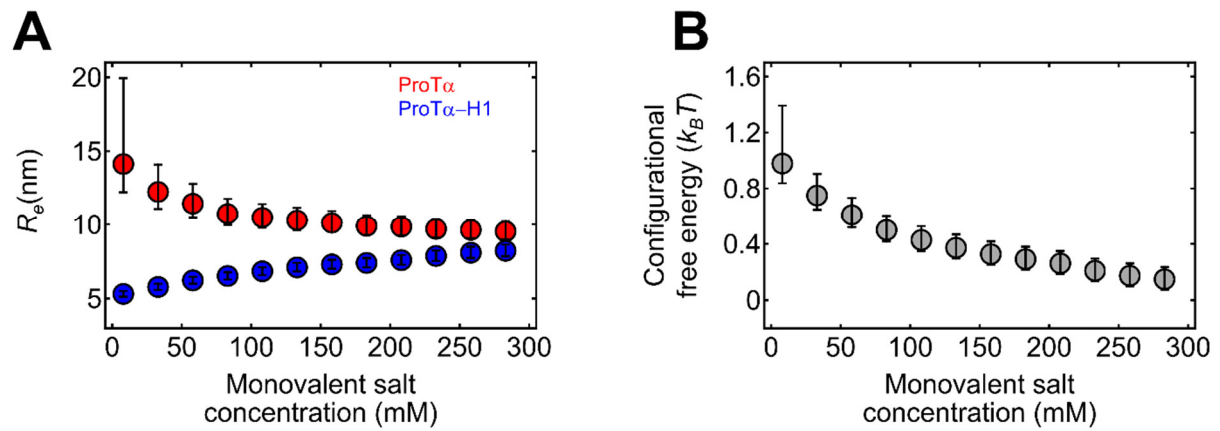
SI Figures and Tables

A

B

Figure S1: (A) R_e for unbound (red) and H1-bound (blue) ProTα as a function of monovalent salt concentration measured using single-molecule FRET with 2C/110C ProTα (in 10 mM Tris buffer, monovalent salt concentration adjusted with KCl). The error bars are estimated from a conservative systematic error ±0.03 on transfer efficiencies. (B) Configurational free energy change of ProTα upon H1 binding estimated from the change in R_e (A) using eq. 9. The error bars represent the error propagated from the errors on R_e (A). Note that the total change in configurational free energy upon binding (for both chains) does not exceed 2 $k_B T$ even in the absence of added salt, where the compaction is maximal.
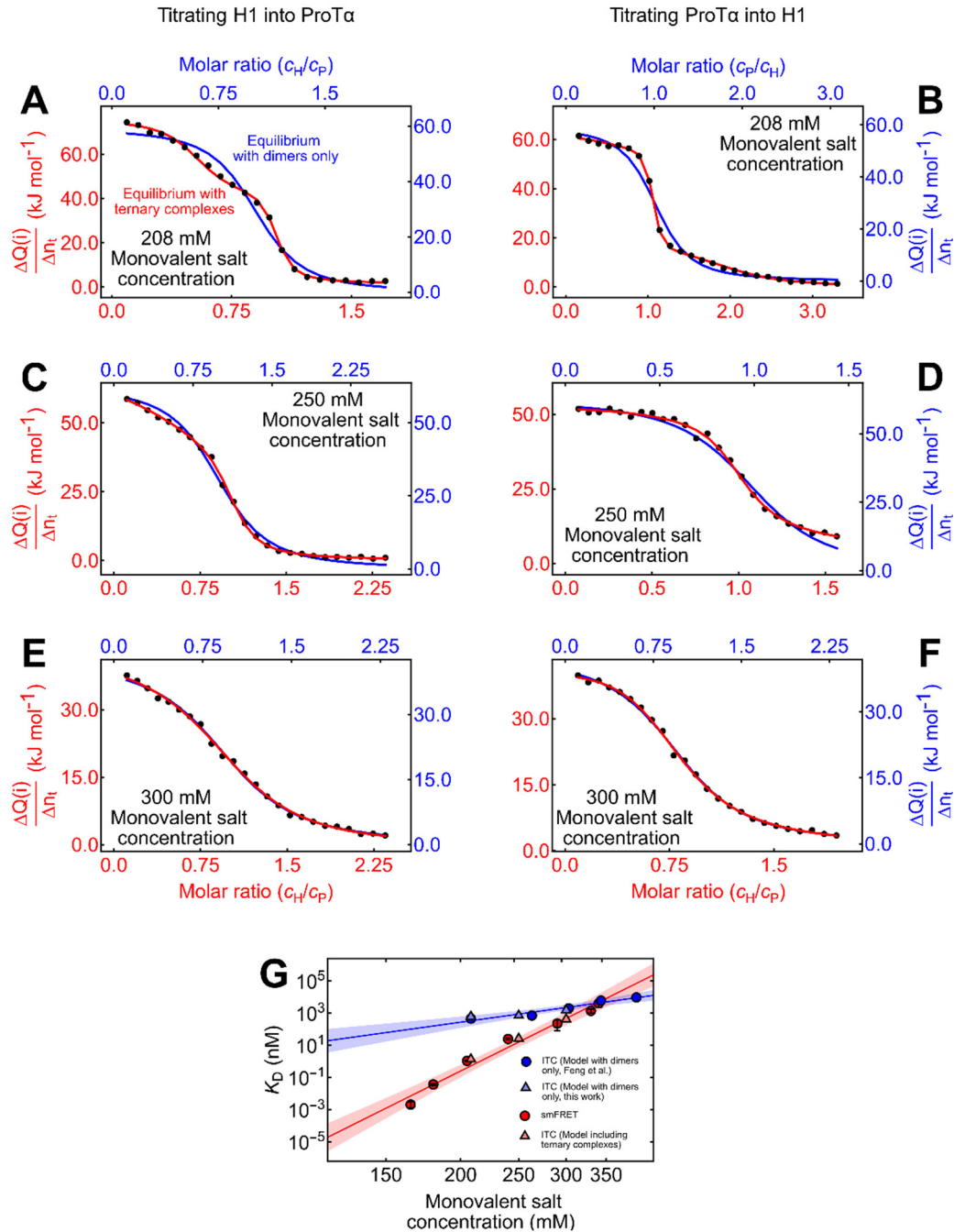
Figure S2: (A-F) Integrated power from ITC per molar amount of injected titrant ($\Delta Q/\Delta n_t$; black points for each injection i) as a function of molar ratio the two proteins upon titrating H1 into ProTα (A, C & E) and titrating ProTα into H1 (B, D & F) at monovalent salt concentrations of 208 mM (A,B), 250 mM (C,D), and 300 mM (E,F). The data in (A-F) are globally fitted either with a 1:1 binding model (blue line and blue axis labels), or with a model including PHH and PPH ternary complexes (red line and axis labels). Note that the molar ratio is a fit parameter and thus slightly different for the two analyses (top and bottom axes). (G) Comparison of the dissociation constants for heterodimer formation from single-molecule FRET and ITC. Circles show K_D^{PH} from single-molecule FRET (red, data and errors from Borgia et al.[2]) and apparent dissociation constants from ITC analyzed with a 2-state model (blue, from Feng et al.[40]). Triangles represent apparent dissociation constants from ITC (A-F) using a 2-state model (blue) or the model including ternary complex formation (red). Solid lines represent fits with Eq. 3 (Main text) and shaded bands the corresponding 90% confidence intervals.
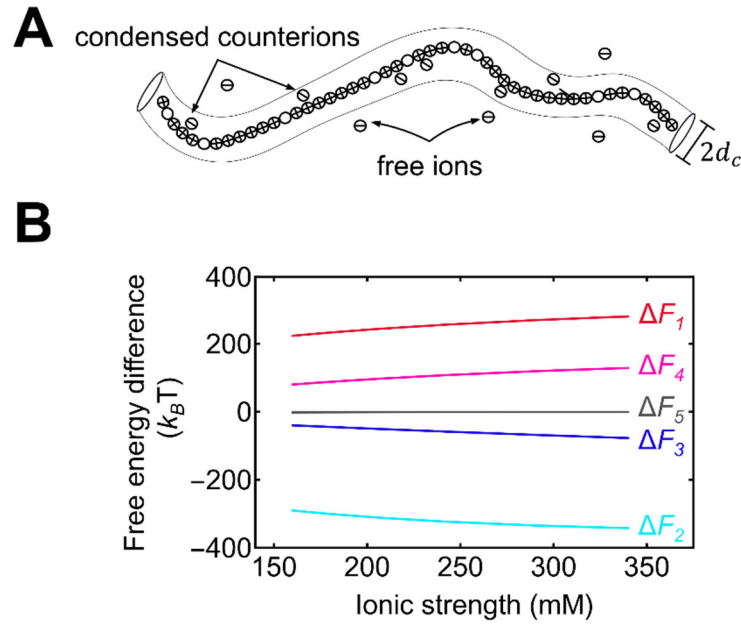
Figure S3: (A) Schematic of the cylindrical volume around the polyions that is used for calculating the local counterion condensation entropy. The radius of the cylinder is taken to be d_c (see text for definition). All counterions inside the cylinder are considered to be condensed to the chain but free to move within the cylinder. (B) Dependence of the differences in the free energy components between uncomplexed and fully complexed chains (components of the free energy of chain complexation), ΔF_1 (entropy of condensed ions), ΔF_2 (entropy of free ions), ΔF_3 (correlation of dissociated ions), ΔF_4 (Coulomb free energy of ion-pair formation), and ΔF_5 (conformational free energy of the chains) on salt concentration, computed using the parameters in Table S5.
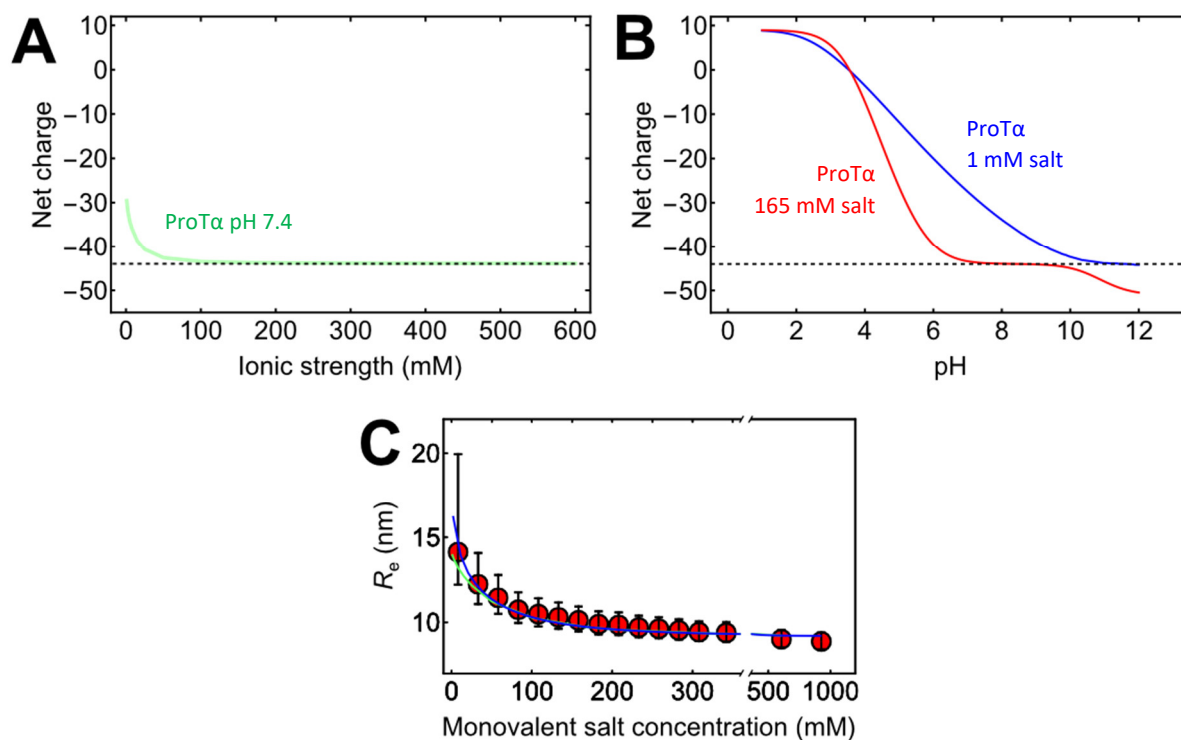
Figure S4: (A, B) Calculations of the salt concentration-dependent net charge of ProTα performed using the pepKalc server (https://st-protein02.chem.au.dk/pepkalc/). (A) Net charge of ProTα at pH 7.4 as a function of ionic strength. The dashed black lines indicate the structural charge based on the tabulated pK_a values of the acidic and basic groups of the free amino acids at pH 7.4. (B) Net charge of ProTα as a function of pH at 1 mM ionic strength (blue curve) and 165 mM ionic strength (red curve). Similar calculations for H1 also indicate recovery of its structural charge at ~100 mM ionic strength. (C) R_e for unbound ProTα as a function of monovalent salt concentration measured using single-molecule FRET with 2C/110C ProTα (filled circles). The error bars are estimated from a conservative systematic uncertainty of ±0.03 on transfer efficiencies. The blue line represents R_e using the theory for a single, isolated polyelectrolyte chain (as in Fig. 4F) using a net charge of -44; the green line represents estimates from the theory where the charge of ProTα was set to the ionic strength-dependent values shown in (A). All parameters except the charge are kept at the values given in Table S5.
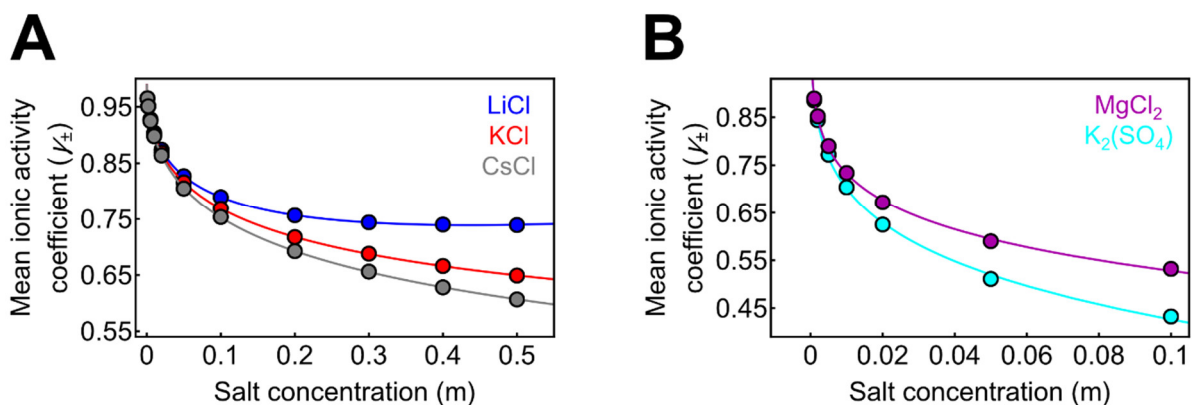
Figure S5: (A) Mean ionic activity coefficients, $\gamma_{\pm}$, as a function of molal concentration of monovalent salts, m, for KCl (red), LiCl (Blue) and CsCl (gray) [12] interpolated with the empirical functions given in Table S4 (lines). **(B)** $\gamma_{\pm}$ as a function of molal concentration of salts with a divalent cation or divalent anion, $MgCl_2$ (magenta) and $K_2(SO_4)$ (cyan), respectively [12], interpolated with the empirical functions given in Table S4 (lines).

Monovalent salt concentration (mM)	Titrant	Apparent K_D (μM)	Apparent ΔH $\left(\dfrac{kJ}{mol}\right)$	% Deviation from nominal titrant concentration	% Deviation from nominal titrand concentration	χ^2
208	ProTα	0.8	59.0	+19.8	-5.2	9.71
208	H1	0.8	59.0	+18.6	+8.9	9.44
250	ProTα	0.9	62.3	-0.9	0.0	5.89
250	H1	0.9	62.3	+20	0.0	3.89
300	ProTα	1.9	42.7	+19.0	-18.4	0.35
300	H1	1.9	42.7	-2.2	-7.2	0.51

Table S1: Parameters obtained from a global fit of the ITC data imposing a 2-state model. Note that we use titrant and titrand concentrations as fit parameters instead of stoichiometry (see Methods).

Monovalent salt concentration (mM)	Titrant	$K_{D(1)}^{PH}$ (nM)	$K_{D(2)}^{PH}$ (nM)	$\lvert\Delta G_{(1)}^{PH} - \Delta G_{(2)}^{PH}\rvert$ ($k_B T$)	$K_{D(1)}^{PPH}$ (μM)	$K_{D(2)}^{PPH}$ (μM)	$\lvert\Delta G_{(1)}^{PPH} - \Delta G_{(2)}^{PPH}\rvert$ ($k_B T$)	$K_{D(1)}^{PHH}$ (μM)	$K_{D(2)}^{PHH}$ (μM)	$\lvert\Delta G_{(1)}^{PHH} - \Delta G_{(2)}^{PHH}\rvert$ ($k_B T$)	ΔH^{PH} $\left(\frac{kJ}{mol}\right)$	ΔH^{PPH} $\left(\frac{kJ}{mol}\right)$	ΔH^{PHH} $\left(\frac{kJ}{mol}\right)$	Deviation from nominal titrant concentration (%)	Deviation from nominal titrand concentration (%)	χ^2
208	ProTα	1.7	0.5	1.2	2.6	3.3	0.2	8.9	14	0.5	58.2	17.6	4.2	+12.9	-16.3	0.38
208	H1	1.7	0.5	1.2	2.6	3.3	0.2	8.9	14	0.5	58.2	17.6	4.2	-5.3	-2.3	0.88
250	ProTα	32	16	0.7	15	14	0.1	7.0	18	0.9	49.8	19.7	2.5	+8.9	+20.0	1.02
250	H1	32	16	0.7	15	14	0.1	7.0	18	0.9	49.8	19.7	2.5	+13.0	-9.4	0.49
300	ProTα	51	470	0.1	150	58	1.0	8.5	23	0.9	36.8	15.9	3.8	+19.0	-10.4	0.28
300	H1	51	470	0.1	150	58	1.0	8.5	23	0.9	36.8	15.9	3.8	-6.7	-2.6	0.39

Table S2: Parameters obtained by globally fitting the ITC data with the complete model including ternary complex formation. $K_{D(1)}^{X}$ and $\Delta G_{(1)}^{X}$ represent values from ITC, and $K_{D(2)}^{X}$ and $\Delta G_{(2)}^{X}$ correspond to values from the extrapolation of salt-dependent dissociation constants (Fig. 4a and Fig. S2). Note that we use titrant and titrand concentrations as fit parameters instead of stoichiometry (see Methods).

Unlabeled ProTα (WT isoform 2)	GPMSDAAVDTSSEITTKDLKEKKEVVEEAENGRDAPANGNANEENGE QEADNEVDEEEEEGGEEEEEEEEGDGEEEDGDEDEEAESATGKRAAE DDEDDDVDTKKQKTDEDD
Labeled ProTα 2C/110C (isoform 1)	GP**C**DAAVDTSSEITTKDLKEKKEVVEEAENGRDAPANGNAENEENGEQ EADNEVDEEEEEGGEEEEEEEEGDGEEEDGDEDEEAESATGKRAAED DEDDDVDTKKQKTDED**C**
Labeled ProTα 2C/110C (isoform 1)	G**C**DAAVDTSSEITTKDLKEKKEVVEEAENGRDAPANGNAENEENGEQE ADNEVDEEEEEGGEEEEEEEEGDGEEEDGDEDEEAESATGKRAAEDD EDDDVDTKKQKTDED**C**GA
Labeled ProTα 56C/110C (isoform 1)	GPSDAAVDTSSEITTKDLKEKKEVVEEAENGRDAPANGNAENEENGEQ EADNEVDEE**C**EEGGEEEEEEEEGDGEEEDGDEDEEAESATGKRAAED DEDDDVDTKKQKTDED**B**
Unlabeled H1	TENSTSAPAAKPKRAKASKKSTDHPKYSDMIVAAIQAEKNRAGSSRQSI QKYIKSHYKVGENADSQIKLSIKRLVTTGVLKQTKGVGASGSFRLAKSD EPKKSVAFKKTKKEIKKVATPKKASKPKKAASKAPTKKPKATPVKKAKK KLAATPKKAKKPKTVKAKPVKASKPKKAKPVKPKAKSSAKRAGKKK

Table S3: Amino acid sequences of the proteins used. Cysteine residues introduced for fluorophore conjugation are highlighted in red. All labeled variants are ProTα isoform 1, while unlabeled ProTα is isoform 2; the isoforms differ by a single glutamate residue at position 39[1]. The two variants of labeled ProTα 2C/110C originate from different expression constructs, but the cysteine positions and the intervening sequences are identical, resulting in experimentally indistinguishable behavior.

Salt	Fit equation	Fit parameters		
		A	B	C
KCl	$\gamma_{+} = 10^{\left[\dfrac{-0.5108\sqrt{\left(\frac{m}{mol\,kg^{-1}}\right)}}{1+B\sqrt{\left(\frac{m}{mol\,kg^{-1}}\right)}}+C\left(\frac{m}{mol\,kg^{-1}}\right)\right]}$	-	1.3198	-0.0014
LiCl		-	1.3440	0.1084
CsCl		-	1.0369	-0.0171
MgCl$_2$	$\gamma_{\pm} = A + C\left(\dfrac{m}{mol\,kg^{-1}}\right)^{B}$	1.4731	0.1061	-1.2068
K$_2$(SO$_4$)		1.3084	0.1623	-1.2818

Table S4: Empirical equations used for fitting mean ionic activity coefficient ($\gamma_{\pm}$) as a function of molal concentration of salts (m), for different salts (Fig. S6), with the resulting fit parameters.

Parameter	Value	Parameter fixed or adjustable	Physical significance of the parameter
N_1	53	Fixed (See discussion on parameterization)	Number of Kuhn segments in the polyelectrolyte chains; N_1 refers to ProTα and N_2 to H1.
N_2	62		
N_{c1}	44	Fixed (See discussion on parameterization)	Charges of the polyelectrolyte chain; N_{c1} refers to ProTα and N_{c2} to H1.
N_{c2}	53		
$\ell\,(nm)$	0.8	Fixed (See discussion on parameterization)	Length of a Kuhn segment
$\tilde{r}_c$	0.3	Fixed (See discussion on parameterization)	The diameter of the counterions divided by the Kuhn segment length. In this case, the diameter of the counterions, r_c, is 0.24 nm.
w_0	1.8	Adjustable (See discussion on parameterization)	Represents the monomer-monomer two-body interaction strengths (inter and intra-chain) and determine the excluded volume in the absence of electrostatics.
δ_0	3.85	Adjustable (See discussion on parameterization)	Represent the dielectric mismatch parameters, which are mean field parameters encompassing two physical quantities, an effective dipole length and a local dielectric constant. This mean field parameter determines the ion pair free energy. (Note that from the theory or the experiments, the local dielectric constant and the dipole length cannot be determined independently.) δ_0 is the dielectric mismatch parameter for ProTα-counterion and H1-counterion pairing, and δ_{12} is the value for ProTα-H1 ion pairing.
δ_{12}	1.8		
Λ	2.0	Adjustable (See discussion on parameterization)	This parameter acts as a multiplicative correction factor to the expression of free energy from ionic correlations using Debye-Hückel screening. It is required since pure Debye-Hückel screening underestimates the free energy from ionic correlations at high salt. See discussion on this correction factor.

Table S5: Parameters used in the theory to calculate the free energy and enthalpy of chain complexation and chain dimensions with their values, nature (free or adjustable), and physical significance.

SI References

1. A Sottini, A Borgia, MB Borgia, K Bugge, D Nettels, A Chowdhury, PO Heidarsson, F Zosel, RB Best, BB Kragelund, & B Schuler (2020) Polyelectrolyte interactions enable rapid association and dissociation in high-affinity disordered protein complexes. *Nat. Commun.* 11:5736.
2. A Borgia, MB Borgia, K Bugge, VM Kissling, PO Heidarsson, CB Fernandes, A Sottini, A Soranno, KJ Buholzer, D Nettels, BB Kragelund, RB Best, & B Schuler (2018) Extreme disorder in an ultrahigh-affinity protein complex. *Nature* 555:61-66.
3. S Müller-Späth, A Soranno, V Hirschfeld, H Hofmann, S Rüegger, L Reymond, D Nettels, & B Schuler (2010) Charge interactions can dominate the dimensions of intrinsically disordered proteins. *Proc. Natl. Acad. Sci. USA* 107:14609-14614.
4. N Galvanetto, MT Ivanović, A Chowdhury, A Sottini, MF Nüesch, D Nettels, RB Best, & B Schuler (2023) Extreme dynamics in a biomolecular condensate. *Nature* 619:876-883.
5. A Chowdhury, SA Kovalenko, IV Aramburu, PS Tan, NP Ernsting, & EA Lemke (2019) Mechanism-Dependent Modulation of Ultrafast Interfacial Water Dynamics in Intrinsically Disordered Protein Complexes. *Angew. Chem. Int. Ed.* 58:4720-4724.
6. V Kudryavtsev, M Sikor, S Kalinin, D Mokranjac, CAM Seidel, & DC Lamb (2012) Combining MFD and PIE for Accurate Single-Pair Förster Resonance Energy Transfer Measurements. *ChemPhysChem* 13:1060-1078.
7. D Nettels, S Müller-Späth, F Küster, H Hofmann, D Haenni, S Rüegger, L Reymond, A Hoffmann, J Kubelka, B Heinz, K Gast, RB Best, & B Schuler (2009) Single molecule spectroscopy of the temperature-induced collapse of unfolded proteins. *Proc. Natl. Acad. Sci. USA* 106:20740–20745.
8. T Yang, J Choo, S Stavrakis, & A de Mello (2018) Fluoropolymer-Coated PDMS Microfluidic Devices for Application in Organic Synthesis. *Chem. Eur. J.* 24:12078-12083.
9. RKP Benninger, Y Koç, O Hofmann, J Requejo-Isidro, MAA Neil, PMW French, & AJ deMello (2006) Quantitative 3D Mapping of Fluidic Temperatures within Microchannel Networks Using Fluorescence Lifetime Imaging. *Anal. Chem.* 78:2272-2278.
10. ED Holmstrom, A Holla, W Zheng, D Nettels, RB Best, & B Schuler (2018) Accurate Transfer Efficiencies, Distance Distributions, and Ensembles of Unfolded and Intrinsically Disordered Proteins From Single-Molecule FRET. *Methods Enzymol.* 611:287-325.
11. K Gast, H Damaschun, K Eckert, K Schulze-Forster, HR Maurer, M Mueller-Frohne, D Zirwer, J Czarnecki, & G Damaschun (1995) Prothymosin .alpha.: A Biologically Active Protein with Random Coil Conformation. *Biochemistry* 34:13211-13218.
12. CRC (2013) *Handbook of Chemistry and Physics* (CRC Press Inc. 2013, Boca Raton).
13. W Zheng, GH Zerze, A Borgia, J Mittal, B Schuler, & RB Best (2018) Inferring properties of disordered chains from FRET transfer efficiencies. *J. Chem. Phys.* 148.
14. M Aznauryan, L Delgado, A Soranno, D Nettels, J-r Huang, AM Labhardt, S Grzesiek, & B Schuler (2016) Comprehensive structural and dynamical view of an unfolded protein from the combination of single-molecule FRET, NMR, and SAXS. *Proc. Natl. Acad. Sci. USA* 113:E5389-E5398.
15. M Rubinstein & RH Colby (2003) *Polymer physics* (Oxford University Press, Oxford ; New York) pp xi, 440 p.
16. MT Record, Jr., CF Anderson, & TM Lohman (1978) Thermodynamic analysis of ion effects on the binding and conformational equilibria of proteins and nucleic acids: the roles of ion association or release, screening, and ion effects on water activity. *Q. Rev. Biophys.* 11:103-178.
17. T Engel & P Reid (Philip Reid) *Physical Chemistry 3rd Editio* (Pearson Education, Inc. 2012).
18. MM Garner & DC Rau (1995) Water release associated with specific binding of gal repressor. *EMBO J.* 14:1257-1263.

19. HP Lehmann, X Fuentes-Arderiu, & LF Bertello (1996) Glossary of terms in quantities and units in Clinical Chemistry (IUPAC-IFCC Recommendations 1996). *Pure Appl. Chem.* 68:957-1000.
20. J Tellinghuisen (2007) Calibration in isothermal titration calorimetry: Heat and cell volume from heat of dilution of NaCl(aq). *Anal. Biochem.* 360:47-55.
21. MicroCal (2014) *ITC200 System User Manual* (Malvern Instruments Ltd.).
22. JD Chodera & DL Mobley (2013) Entropy-Enthalpy Compensation: Role and Ramifications in Biomolecular Ligand Recognition and Design. *Annu. Rev. Biophys.* 42:121-142.
23. J Tellinghuisen & JD Chodera (2011) Systematic errors in isothermal titration calorimetry: Concentrations and baselines. *Anal. Biochem.* 414:297-299.
24. H Naghibi, A Tamura, & JM Sturtevant (1995) Significant discrepancies between van't Hoff and calorimetric enthalpies. *Proc. Natl. Acad. Sci. USA* 92:5597-5599.
25. S Mitra & A Kundagrami (2023) Polyelectrolyte complexation of two oppositely charged symmetric polymers: A minimal theory. *J. Chem. Phys.* 158:014904.
26. S Ghosh, S Mitra, & A Kundagrami (2023) Polymer complexation: Partially ionizable asymmetric polyelectrolytes. *J. Chem. Phys.* 158:10.1063/1065.0147323.
27. SF Edwards & P Singh (1979) Size of a polymer molecule in solution. Part 1.—Excluded volume problem. *J. Chem. Soc., Faraday Trans. 2* 75:1001-1019.
28. M Muthukumar (1987) Adsorption of a polyelectrolyte chain to a charged surface. *J. Chem. Phys.* 86:7230-7235.
29. M Muthukumar (2004) Theory of counter-ion condensation on flexible polyelectrolytes: adsorption mechanism. *J. Chem. Phys.* 120:9343-9350.
30. M Muthukumar (2023) *Physics of Charged Macromolecules: Synthetic and Biological Systems* (Cambridge University Press, Cambridge).
31. A Kundagrami & M Muthukumar (2010) Effective Charge and Coil−Globule Transition of a Polyelectrolyte Chain. *Macromolecules* 43:2574-2581.
32. R Kjellander (2020) A multiple decay-length extension of the Debye–Hückel theory: to achieve high accuracy also for concentrated solutions and explain under-screening in dilute symmetric electrolytes. *Phys. Chem. Chem. Phys.* 22:23952-23985.
33. PJ Flory & WR Krigbaum (2004) Statistical Mechanics of Dilute Polymer Solutions. II. *J. Chem. Phys.* 18:1086-1094.
34. DA McQuarrie (1975) *Statistical Mechanics* (Harper & Row).
35. H Hofmann, A Soranno, A Borgia, K Gast, D Nettels, & B Schuler (2012) Polymer scaling laws of unfolded and intrinsically disordered proteins quantified with single-molecule spectroscopy. *Proc. Natl. Acad. Sci. USA* 109:16155-16160.
36. M Doi (1996) *Introduction to polymer physics* (Oxford university press).
37. K Tamiola, RM Scheek, P van der Meulen, & FAA Mulder (2018) pepKalc: scalable and comprehensive calculation of electrostatic interactions in random coil polypeptides. *Bioinformatics* 34:2053-2060.
38. MAS Hass & FAA Mulder (2015) Contemporary NMR Studies of Protein Electrostatics. *Annu. Rev. Biophys.* 44:53-75.
39. BJ Payliss, J Vogel, & AK Mittermaier (2019) Side chain electrostatic interactions and pH-dependent expansion of the intrinsically disordered, highly acidic carboxyl-terminus of γ-tubulin. *Protein Sci.* 28:1095-1105.
40. H Feng, BR Zhou, & Y Bai (2018) Binding Affinity and Function of the Extremely Disordered Protein Complex Containing Human Linker Histone H1.0 and Its Chaperone ProTalpha. *Biochemistry* 57:6645-6648.